Divalent cations influence the dimerization mode of murine S100A9 protein by modulating its disulfide bond pattern

Luca Signor, Theo Paris, Caroline Mas, Adrien Picard, Georges Lutfalla, Elisabetta Boeri Erba, Laure Yatime

Divalent cations influence the dimerization mode of murine S100A9 protein by modulating its disulfide bond pattern

Author names

Luca Signor[1], Theo Paris[2], Caroline Mas[3], Adrien Picard[2], Georges Lutfalla[2], Elisabetta Boeri Erba[1,*], Laure Yatime[4,*]

Author affiliations

[1] Univ. Grenoble Alpes, CEA, CNRS, IBS, F-38000 Grenoble, France

[2] LPHI UMR5235, Univ. Montpellier, CNRS, F-34095 Montpellier, France

[3] ISBG UMS 3518, CNRS, CEA, Univ. Grenoble Alpes, EMBL, F-38000 Grenoble, France

[4] LPHI UMR5235, Univ. Montpellier, CNRS, INSERM, F-34095 Montpellier, France

*** Correspondence to:**

Dr. Laure Yatime; laure.yatime@inserm.fr or Dr. Elisabetta Boeri Erba; elisabetta.boeri-erba@ibs.fr

Highlights

The crystallographic structure of mS100A9 bound to calcium and zinc is reported

A novel Zn-binding site and a disulfide bridge rigidify mS100A9 C-terminus

In solution, mS100A9 exists both as non-covalent and disulfide-crosslinked homodimers

Divalent cations modulate the relative proportion of the different mS100A9 homodimers

Abstract

S100A9, with its congener S100A8, belongs to the S100 family of calcium-binding proteins found exclusively in vertebrates. These two proteins are major constituents of neutrophils. In response to a pathological condition, they can be released extracellularly and become alarmins that induce both pro- and anti-inflammatory signals, through specific cell surface receptors. They also act as antimicrobial agents, mainly as a S100A8/A9 heterocomplex, through metal sequestration. The mechanisms whereby divalent cations modulate the extracellular functions of S100A8 and S100A9 are still unclear. Importantly, it has been proposed that these ions may affect both the ternary and quaternary structure of these proteins, thereby influencing their physiological properties. In the present study, we report the crystal structures of WT and C80A murine S100A9 (mS100A9), determined at 1.45 and 2.35 Å resolution, respectively, in the presence of calcium and zinc. These structures reveal a canonical homodimeric form for the protein. They also unravel an intramolecular disulfide bridge that stabilizes the C-terminal tail in a rigid conformation, thus shaping a second Zn-binding site per S100A9 protomer. In solution, mS100A9 apparently binds only two zinc ions per homodimer, with an affinity in the micromolar range, and aggregates in the presence of excess zinc. Using mass spectrometry, we demonstrate that mS100A9 can form both non-covalent and covalent homodimers with distinct disulfide bond patterns. Interestingly, calcium and zinc seem to affect differentially the relative proportion of these forms. We discuss how the metal-dependent interconversion between mS100A9 homodimers may explain the versatility of physiological functions attributed to the protein.

Keywords

S100 proteins; divalent cations; disulfide bridges; X-ray crystallography; mass spectrometry.

Abbreviations

alk: alkylation; ACN: acetonitrile; DTT: dithiothreitol; HPLC: high performance liquid chromatography; IAA: iodoacetamide; hS100A9: human S100A9; ICP-MS: Inductively-coupled plasma mass spectrometry; LC/ESI-TOF-MS: liquid chromatography/electrospray ionization time-of-flight mass spectrometry; MPD: 2-Methyl-2,4-pentanediol; MR: molecular replacement; mS100A9: murine S100A9; RAGE: receptor for advanced glycation end-products; r.m.s.d.: root mean square deviation; SEC: size exclusion chromatography; TFA: trifluoroacetic acid; TLR: Toll-like receptor; WT: wild-type.

1. Introduction

S100 proteins are a group of small Ca^{2+}-binding proteins expressed exclusively in vertebrates (Marenholz et al., 2004; Donato et al., 2013; Gonzalez et al., 2020). Several members of this family also exist extracellularly where they act as alarmins and thereby play a crucial role in the modulation of inflammatory responses in various disease contexts, through their interactions with cell surface receptors such as the receptor for advanced glycation end-products (RAGE), Toll-like receptors (TLRs) or various cluster of differentiation molecules (Leclerc et al., 2011; Roh et al., 2018; Gonzalez et al., 2020).

S100A9, also known as calgranulin B or migration inhibitory factor-related protein 14 (MRP14), is one of the most well-studied members among this large family of proteins encoded by up to thirty genes (Kraemer et al., 2008; Gonzalez et al., 2020). *In vivo*, S100A9 is mostly present as a heterodimer with its congener S100A8 (aka calgranulin A or MRP8) (Longbottom et al., 1992). The extracellular form of this heterodimer is known as calprotectin. Homodimers of both proteins are also detected to some extent, but they seem to be much less stable than the heterodimeric form (Hunter et al., 1998; Kallberg et al., 2018; Wang et al., 2018b; Giudice et al., 2019). S100A8 and S100A9 are highly expressed in circulating neutrophils, as well as in monocytes (Lagasse et al., 1992; Striz et al., 2004). They can constitute up to 45% of the total cytosolic pool of proteins in these cells, being found either in the cytoplasm or associated with the plasma membrane (Striz et al., 2004; Wang et al., 2018b). Intracellularly, S100A8/A9 act as Ca^{2+}-sensors. In response to an increase in calcium levels, they regulate various processes including cytoskeleton rearrangement, cell migration, phagocytosis, exocytosis, and respiratory burst, the latter through the delivery of arachidonic acid to the membrane-bound NADPH oxidase (Goebeler et al., 1995; Kerkhoff et al., 2005; Wang et al., 2018b). In a pathological context, S100A8/A9 can be released in the extracellular space by

infiltrating leukocytes or following cell necrosis. Once these S100 proteins are outside the cells, their functions change dramatically: they mainly act as damage-associated molecular patterns (DAMPs), promoting leukocyte recruitment through chemotaxis and massive production of pro-inflammatory cytokines via their interactions with specific cell surface receptors. These processes participate in the maintenance of a high inflammatory state which aggravates the underlying pathology that led to S100 protein release (Wang et al., 2018b; Gonzalez et al., 2020). S100A8 and S100A9 have been shown to bind to both RAGE, TLR4, CD147, and neuroplastin (Sakaguchi et al., 2016; Ma et al., 2017). Many other yet unraveled receptors may also serve as transducers of the pro-inflammatory signals elicited by the extracellular heterodimer and/or homodimers (Tomonobu et al., 2020). S100A8/A9 signaling has been linked to a plethora of inflammatory or inflammation-driven pathologies, including rheumatoid arthritis, myocardial infarction, Alzheimer's disease or cancers (Shabani et al., 2018; Wang et al., 2018a; Marinkovic et al., 2019; Wang et al., 2019). These two S100 proteins are therefore considered as valuable therapeutic targets (Bjork et al., 2009; Reeb et al., 2015; Pruenster et al., 2016). They are also utilized as biomarkers for the diagnostic of certain pathologies such as inflammatory bowel diseases, due to their increased plasma levels in an inflammatory context (Chaabouni et al., 2016).

S100 proteins fold into a four-helix globular domain that is sometimes followed by a C-terminal, unstructured extension of variable length (Donato et al., 2013). The minimal functional unit is a homo- or heterodimer, but higher order oligomers are also encountered (Leukert et al., 2006). As for other S100 proteins, S100A9 active conformation requires the presence of two Ca^{2+} ions, one in each EF-hand motif, for proper effector binding (Vogl et al., 2006). In addition to calcium, both human and murine S100A9 were shown to bind zinc (Raftery et al., 1996). Many S100 proteins possess two symmetrical Zn^{2+} binding motifs located at the interface between the two subunits of the S100

112 homodimer (Brodersen et al., 1999; Moroz et al., 2009a; Lin et al., 2016). These tetrahedral binding
113 sites are formed by two histidine residues (or possibly an aspartic acid replacing the second His)
114 surrounding the first EF-hand motif of one protomer, and two histidine residues (or equivalent
115 positively charged residues) placed at the C-terminal end of the fourth helix in the second protomer.
116 S100 proteins can also chelate other divalent cations such as manganese, iron, nickel or copper
117 (Nakashige et al., 2015; Zackular et al., 2015; Gilston et al., 2016; Nakashige et al., 2017). Chelation
118 of Mn^{2+}, Ni^{2+} and Fe^{2+} by S100A8/A9 is part of a sequestration process known as nutritional
119 immunity that aims at depriving invading pathogens from these essential nutrients (Damo et al.,
120 2013; Nakashige et al., 2015; Nakashige et al., 2017). Thanks to the patch of histidine residues
121 located in the long, flexible C-terminal tail of its S100A9 moiety, the S100A8/A9 heterodimer can
122 generate an octahedral His_6 binding motif for Mn^{2+}/Ni^{2+} coordination, thereby increasing the affinity
123 of the protein for these metal ions (Damo et al., 2013; Nakashige et al., 2018). Therefore,
124 S100A8/A9 is considered as a potent antimicrobial peptide (Corbin et al., 2008). Other S100 proteins
125 have been shown to possess bactericidal properties (Glaser et al., 2005; Realegeno et al., 2016), but
126 it is not known whether S100A9 also displays such ability to kill bacteria outside the S100A8/A9
127 heterodimer (i.e. as a homodimer).

128 Metal ion chelation by S100 proteins may however not be restricted to an antimicrobial activity.
129 Indeed, divalent cations other than calcium may act as modulators of the biological function of S100
130 proteins, in particular zinc (Baudier et al., 1986; Nakatani et al., 2005; Moroz et al., 2011). Various
131 processes may induce modifications in the structural organization of S100 proteins, including ion
132 binding, which promotes protein oligomerization, as well as post-translational modifications and/or
133 oxidation-dependent mechanisms that may lead for example to the formation of disulfide-
134 crosslinked S100 oligomers having distinct functions than the non-covalent assemblies

(Winningham-Major et al., 1989; Haase-Kohn et al., 2011; Lim et al., 2011; Unno et al., 2011; Yatime, 2017). We and others have proposed that these effects may be the direct translation of a change in S100 proteins tertiary and/or quaternary structure (Moroz et al., 2009b; Yatime et al., 2016). Although these ideas are generally more and more well perceived by the scientific community working in the field, these forms have so far not been characterized in details. To date, only one structural study reports the finding of a novel homodimeric form of S100 proteins, observed for S100A6 in its complex with RAGE and stabilized by zinc and cysteine-dependent mechanisms (Yatime et al., 2016). In order to understand how these proteins can have many diverse and sometimes contradictory functions, differences between species should also be taken into account. For example, the C-terminal region of murine S100A9 (mS100A9) was shown to have antinociceptive functions and to inhibit macrophage functions through modulation of B1 cell function (Paccola et al., 2008; Pagano et al., 2014). Remarkably, these properties have so far not been ascribed to the human protein. Such distinct properties may arise from local differences in the 3D-architectures of human and murine proteins, possibly driven by divalent cations since S100A9 C-terminal region has been involved in metal chelation, at least as part of the S100A8/A9 heterocomplex (Damo et al., 2013; Nakashige et al., 2015).

In order to gain deeper insight on how divalent cations may act as regulators of these processes at a structural level, we have undertaken the biophysical characterization of mS100A9 in the presence of various sets of cations. Using X-ray crystallography and mass spectrometry, we show that the mS100A9 homodimers exist, in solution, both as non-covalent and covalent, disulfide-crosslinked forms. The non-covalent homodimers contain an intramolecular disulfide bridge linking Cys91 to Cys111. The disulfide-crosslinked homodimers are characterized by distinct disulfide bond patterns depending on the metal present. We also demonstrate that the relative proportion of these

158 forms depends on the ions bound to the protein. Calcium appears to promote the non-covalent,
159 canonical homodimer, whereas zinc enhances the formation of the SS-bridged homodimer(s).
160 Furthermore, we observe that the C-terminal region of mS100A9 contains an additional Zn^{2+}
161 binding site, distinct from the one at the interface between the two monomers that is generally
162 observed in the canonical S100 homodimers. Finally, we provide isothermal titration calorimetry
163 (ITC) analyses of zinc binding to mS100A9 and dynamic light scattering (DLS) studies of the
164 zinc-dependent aggregation of mS100A9. All these findings suggest that divalent cations may
165 drastically affect the local conformation of mS100A9 C-terminal tail. In the present study, we
166 discuss the possible consequences of these structural modulations in terms of physiological
167 function.

168 **2. Material and Methods**

169 ***2.1. Expression and purification of mS100A9 WT and mutant proteins***

170 The gene coding for WT mS100A9, optimized for codon usage in *E. coli*, was synthesized by
171 Genscript and further cloned into the *NcoI – HindIII* fragment of vector pETM11 (EMBL vector
172 collection). The protein sequence of the mS100A9 sample obtained with this construct after
173 purification is indicated in Supplementary Table S1. A theoretical molecular weight of 13177 Da
174 is expected. Cysteine-to-alanine point mutants C80A, C91A and C111A, were obtained by PCR-
175 based site-directed mutagenesis using High Fidelity Hot Start Phusion DNA Polymerase
176 (Finnzymes) and anti-complementary oligonucleotides bearing the mutation to introduce
177 (Supplementary Table S1). The resulting mS100A9:pETM11 constructs were used to transform
178 *E. coli* BL21 (DE3) cells. Protein expression and purification was carried out as described
179 previously (Yatime, 2019). Transformed cells were grown at 37ºC for 4 hours and protein
180 expression was induced overnight at 18ºC by adding 1 mM IPTG in the culture medium. Cells

were harvested by centrifugation at 6000 g and disrupted by sonication. After clarification by centrifugation, the cell lysate was loaded onto a 5 ml HisTrap Ni-column (GE Healthcare) equilibrated with 50 mM Tris-HCl pH 7.5, 300 mM NaCl, 30 mM imidazole, 1 mM PMSF. Following high salt wash with a buffer containing 1 M NaCl, to remove nonspecifically bound contaminants, the protein of interest was eluted with a buffer containing 500 mM imidazole. The N-terminal polyhistidine tag was then removed overnight by incubating the sample at 4ºC with home-made recombinant Tobacco Etch Virus protease (rTEV), using a protein to rTEV massic ratio of 30 to 1. A second step of affinity chromatography on the His-Trap Ni-column was then performed to separate the cleaved mS100A9 protein, eluting in the flow-through, from the His_6-tag and His-tagged rTEV that remained bound to the column. 10 mM EDTA/EGTA were then added to the sample to remove all traces of divalent cations and, after overnight incubation with the chelating agents, the protein was further purified by size exclusion chromatography (SEC) on a 24 ml Superdex 75 Increase column (GE Healthcare) equilibrated with Buffer 1 (20 mM Tris-HCl pH 7.5, 100 mM NaCl). Fractions corresponding to the dimeric form of mS100A9 were pooled and the purity of the sample was verified by SDS-PAGE (Supplementary Fig. S1A). The purified mS100A9 homodimer was flash frozen in liquid nitrogen and stored at -80°C until use. This purification protocol yielded in routine 10 mg of pure mS100A9 homodimer per liter of culture.

Before biophysical analyses, mS100A9 samples (WT and mutants) were freshly repurified on a Superdex 75 Increase SEC column equilibrated with Buffer 1, to ensure that a homogenous dimeric form of the protein was used (Supplementary Fig. S1B). SEC was performed at 18ºC, at a flow rate of 0.4 ml/min. 2.5 mg of mS100A9 dimeric pool were injected per run (loading volume: 400 µl of protein concentrated at 6.2 mg/ml). After pooling again the dimeric peak of mS100A9 and

concentrating, the different samples were prepared by incubating mS100A9 at a final protein concentration of 4.8 mg/ml (365 μM) with either 1 mM $CaCl_2$ (mS100A9 + Ca), 1 mM $ZnCl_2$ (mS100A9 + Zn) or 1 mM $CaCl_2$ + 1 mM $ZnCl_2$ (mS100A9 + Ca/Zn), while the apo mS100A9 sample did not contain any of these metals (as assessed by ICP-MS, Table 3). To prepare samples for MS analysis, these stock solutions were further diluted to a final mS100A9 concentration of 50 μM.

2.2. Crystallization, data collection and refinement

Initial crystallization screening was performed by hand using the sitting-drop vapor diffusion technique at 18ºC in 96-well Swissci MRC crystallization plates and commercial screens from Molecular Dimensions Ltd. mS100A9 (WT and C80A) crystallized at 10 mg/ml (760 μM) in the presence of 5 mM $CaCl_2$ (6.6 eq) / 2 mM $ZnCl_2$ (2.6 eq) over a reservoir containing 0.2 M Ammonium sulfate, 4 mM spermine tetrahydrochloride, 50 mM Bis-Tris pH 7.0, 45% MPD. Crystals were directly flash frozen in liquid nitrogen and all datasets (native and anomalous) were collected at 100K on beamline ID23eh1 at ESRF (Grenoble, France) or beamline X06DA at SLS (Villingen, Switzerland). Datasets were processed with XDS (Kabsch, 2010) and the structure was determined by molecular replacement (MR) in PHASER (McCoy et al., 2007), using the structure of Ca^{2+}-bound human S100A9 (PDB_ID 1IRJ) (Itou et al., 2002) for the WT protein, and the newly determined structure of WT mS100A9 for the C80A mutant. Refinement of the models was carried out by alternating cycles of manual rebuilding in COOT (Emsley et al., 2004) and cycles of energy minimization in PHENIX.REFINE (Adams et al., 2010) including refinement of individual isotropic Atomic Displacement Parameters (ADP) using Translation–Libration–Screw (TLS) parameterization (Table 1 and Supplementary Table S2). The quality of the final models was

assessed with MOLPROBITY (Davis et al., 2007). All figures were made with the Pymol Molecular Graphics System (version 0.99rc6, DeLano Scientific LLC).

2.3. Inductively-coupled plasma mass spectrometry (ICP-MS)

The metal content of our protein preparation of WT mS100A9 was analyzed by ICP-MS prior to cation binding studies. A 200 µM stock solution of WT mS100A9 in Buffer 1 was used for measurements. Trace element concentrations were determined both in Buffer 1 alone and in the mS100A9 sample, with the Thermo Scientific iCAP TQ ICP-MS system (using the Kinetic Energy Discrimination mode and He as collision gas) on the AETE-ISO platform (OSU OREME, University of Montpellier, France). An internal solution, containing Be, Sc, Ge, Rh was added on-line to the samples to correct signal drifts. Certified water SLRS-6 (National Research Council of Canada, Metrology Research Centre) was used as a control of the correctness of the measurements.

2.4. Isothermal titration calorimetry (ITC)

The affinity of mS100A9 for $ZnCl_2$ in the presence or absence of $CaCl_2$ was determined using a MicroCal iTC200 system (Malvern Panalytical, Malvern, UK). Experiments were performed at 25ºC in 20 mM Tris-HCl pH 7.5, 100 mM NaCl, +/- 1 mM $CaCl_2$. The mS100A9 protein solution (at concentrations ranging from 30 µM to 120 µM) was loaded in the calorimetric cell. $ZnCl_2$ (at concentrations ranging between 0.6 and 1.2 mM) was titrated in the protein sample typically by performing 16 injections of 2.5 µL or 20 injections of 2 µL each. The dissociation constant (K_d), enthalpy of binding (ΔH), and stoichiometry (N) were obtained after fitting the integrated and normalized data to a single-site binding model. The data were processed using Origin 7.0 (Malvern

Panalytical, Malvern, UK). All experiments were performed at least in duplicate to check for reproducibility of the data.

2.5. Dynamic light scattering (DLS)

DLS measurements were performed at 20ºC using a Zetasizer Nano S from Malvern Instruments Ltd using a quartz cuvette from Hellma Analytics. We measured the hydrodynamic radius (Rh) of the protein mS100A9 at 120 μM, in the presence or absence of 1 mM $CaCl_2$, at different mS100A9 to $ZnCl_2$ molar ratios (1:0, 1:1, 1:2, 1:3 and 1:4).

2.6. Liquid chromatography/electrospray-ionization mass spectrometry (LC/ESI-TOF-MS)

The disulfide bond pattern of mS100A9 in the presence or absence of different divalent cations was investigated by Liquid Chromatography/Electrospray Ionization Mass Spectrometry (LC/ESI-TOF-MS) on a 6210 TOF mass spectrometer coupled to a HPLC system (1100 series, Agilent Technologies). The mass spectrometer was calibrated with tuning mix (ESI-L, Agilent Technologies). The following instrumental settings were used: gas temperature (nitrogen) 300 °C, drying gas (nitrogen) 7 L min−1, nebulizer gas (nitrogen) 10 psig, V_{cap} 4 kV, fragmentor 250 V, skimmer 60 V, V_{pp} (octopole RF) 250 V. The HPLC mobile phases were prepared with HPLC grade solvents. Mobile phase A composition was: H_2O 95%, ACN 5%, TFA 0.03%. Mobile phase B composition was: ACN 95%, H_2O 5%, TFA 0.03%.

For MS analysis of the intact protein, three different samples were prepared for each set of ions: 1) *no treatment*: the protein sample at 10 μM concentration in the corresponding buffer, without any chemical treatment; 2) *alkylation (IAA)*: the protein sample at 10 μM concentration, after incubation with 55 mM IAA (30 min at room temperature, in the dark); 3) *reduction and alkylation (DTT+IAA)*: the protein sample at 10 μM concentration, first incubated with 10 mM DTT (45 min at 56ºC, under gentle mixing) followed by treatment with 55 mM IAA (30 min at room

temperature, in the dark). For the mS100A9 protein without ions, a fourth sample was prepared: 4) *unfolding, reduction and alkylation (urea+DTT+IAA)*: the protein sample at 10 μM concentration, first incubated with 10 mM DTT in the presence of 8 M urea (45 min at 56ºC, under gentle mixing) followed by treatment with 55 mM IAA (30 min at room temperature, in the dark). 2 μl of each protein sample (20 pmol) were injected for MS analysis and were first desalted on-line for 3 min with 100% of mobile phase A (flow rate of 50 μl/ min), using a C8 reverse phase micro-column (Zorbax 300SB-C8, 5μm, 5 × 0.3 mm, Agilent Technologies). The sample was then eluted with 70% of mobile phase B (flow rate of 50 μl/ min) and MS spectra were acquired in the positive ion mode in the 300-3000 *m/z* range. Data were processed with MassHunter software (v. B.02.00, Agilent Technologies) and GPMAW software (v. 7.00b2, Lighthouse Data, Denmark). The mass accuracy on the experimental mass values obtained for the mS100A9 samples from ESI mass spectra, after deconvolution, was of ± 0.06 Da (for the "monomeric" peak) and of ± 0.2 Da (for the "dimeric" peak). To verify whether monomeric and dimeric species have similar relative ionization efficiencies, we assessed the relative ionization efficiency of mS100A9 mutants C111A (that gives only monomeric species) and C91A (that gives only dimeric species). The results, displayed in Supplementary Figure S9, show that both species have relatively similar ionization efficiencies with an estimated average percent error of 5% max, which we consider acceptable. Based on these results, we then evaluated the relative proportions of monomeric and dimeric species in our LC/ESI-TOF MS experiments by measuring the peak area of each species in the deconvoluted ESI MS spectra and reporting their values as a percentage of the sum of all species observed (area % of deconvoluted peak) (see for ex. Figures 4A and 5A). The number of disulfide bonds versus free cysteines was determined for each set of ions by comparing the ESI MS spectra

recorded for the samples without any chemical treatment, with those after reaction with IAA alone or DTT + IAA.

2.7. Native mass spectrometry

The samples were analyzed by native mass spectrometry (Boeri Erba et al., 2015; Boeri Erba et al., 2018; Boeri Erba et al., 2020). Protein ions were generated using a nanoflow electrospray (nano-ESI) source. Nanoflow platinum-coated borosilicate electrospray capillaries were bought from Thermo Electron SAS (Courtaboeuf, France). MS analyses were carried out on a quadrupole time-of-flight mass spectrometer (Q-TOF Ultima, Waters Corporation, Manchester, U.K.). The instrument was modified for the detection of high masses (Sobott et al., 2002; van den Heuvel et al., 2006). The following instrumental parameters were used: capillary voltage = 1.2-1.3 kV, cone potential = 40 V, RF lens-1 potential = 40 V, RF lens-2 potential = 1 V, aperture-1 potential = 0 V, collision energy = 30-140 V, and microchannel plate (MCP) = 1900 V. All mass spectra were calibrated externally using a solution of cesium iodide (6 mg/mL in 50% isopropanol) and were processed with the Masslynx 4.0 software (Waters Corporation, Manchester, U.K.) and with Massign software package (Morgner et al., 2012).

3. Results

3.1. General overview of the Ca^{2+}/Zn^{2+}-bound mS100A9 structure

To date, no structural data on mS100A9 are available. Quite a few structures of hS100A9 are deposited in the Protein Data Bank (PDB), either for the homodimeric form of the protein or for the S100A8/A9 heterotetramer (Itou et al., 2002; Korndorfer et al., 2007; Chang et al., 2016). However, none of these structures has been obtained in the presence of zinc. In fact, the sole information that may be derived on zinc chelation by S100A9 arise from the structures of manganese- and nickel-bound human S100A8/A9 (Damo et al., 2013; Gagnon et al., 2015;

Nakashige et al., 2017; Nakashige et al., 2018). No such data exist for the S100A9 homodimer, although this form is able to bind zinc as well (Raftery et al., 1999). Furthermore, differences in metal coordination between the human and murine proteins cannot be excluded. We therefore started investigating zinc binding to mS100A9 from a structural point of view. As for hS100A9, mS100A9 tends to form higher oligomers than just simple homodimers, as we indeed observed when we analyzed the concentrated protein by size exclusion chromatography (SEC) (Supplementary Figs. S1A and S1C-D). To avoid adding a level of complexity to the study, we focused our experiments on the dimeric pool of the protein, collected separately from the SEC column and rerun after long term storage at -80ºC on the same column to evaluate its stability (Supplementary Fig. S1B). Despite extensive efforts, we could only obtain crystals of the protein in the presence of calcium and zinc. No crystals appeared if any of the two ions was absent from the protein buffer. The crystals belonged to space group C2 and diffracted to a maximum resolution of 1.45 Å (Table 1). The structure was determined by molecular replacement using calcium-bound hS100A9 (Itou et al., 2002) as the MR search model.

The final refined atomic model for Ca^{2+}/Zn^{2+}-bound mS100A9 is displayed in Figure 1A (Table 1 for data statistics). Quality of the fit between this model and the experimental electron density map can be assessed in Figure 1B. As expected, mS100A9 arranges in a centro-symmetrical homodimer that corresponds to the canonical dimer reported for all other S100 proteins. Both subunits bind two calcium ions, in the two EF-hand motifs, and more surprisingly, two zinc ions, one at the interface between the two subunits and one within the C-terminal tail. The exact nature of these ions was confirmed by calculating anomalous difference Fourier maps from datasets collected at the Zn peak (wavelength of 1.27 Å), where both Zn and Ca display anomalous scattering of X-

rays, and just after the Zn peak (wavelength of 1.30 Å), where Zn anomalous signal is lost whereas calcium anomalous signal increases (Fig. 1C).

The overall architecture of mS100A9 closely resembles that of hS100A9. As depicted in Figure 1D, the mS100A9 protomer (beige) superimposes quite well with the corresponding Ca^{2+}-bound protomer of both WT (blue) and C3S (red) hS100A9 homodimer (Itou et al., 2002; Chang et al., 2016) as well as with the Ca^{2+}/Mn^{2+}-bound hS100A9 moiety (grey) of the hS100A8/A9 heterocomplex (Damo et al., 2013). An overall r.m.s.d. on Cα atoms of 1.05 and 1.42 Å can be measured between the murine protein and the WT or mutated hS100A9, respectively, for the core region encompassing helices H1 to H4 (Fig. 1D). Similarly, r.m.s.d. values on Cα atoms comprised between 1.19 and 1.31 Å were obtained by comparing mS100A9 and the hS100A9 moiety from the different human S100A8/A9 structures. The major movements between these structures occur in the second half of helix H4 and in the C-terminal tail of the protein (Fig. 1D), a region that is not modeled in all available structures due to its high flexibility. In mS100A9, the long C-terminal tail adopts a rigidified architecture that will be discussed in more details below.

In contrast to the conserved conformation of the S100A9 protomer observed between human and murine proteins, the respective position of the two mS100A9 subunits within the homodimer differs quite substantially from what is observed for the Ca^{2+}-bound hS100A9 homodimers (Fig. 1E). Indeed, subunit B of mS100A9 is shifted away from subunit A by a rotation of approximately 30º as compared to the equivalent subunits in both structures of the hS100A9 homodimer (Fig. 1E). This differential positioning of the two S100A9 subunits may reflect intrinsic differences between the two S100A9 orthologues. Another possibility is that zinc binding triggers the reorientation of the two S100 subunits. To address this question, we then compared the relative orientation of the two S100 subunits in our Ca^{2+}/Zn^{2+}-bound mS100A9 homodimer with that of

other S100 homodimers bound to calcium alone or to calcium plus zinc. As depicted in Figure 1F and Supplementary Figure S2, our mS100A9 homodimer superimposes quite well with the hS100A7 (Brodersen et al., 1999), hS100A8 (Ishikawa et al., 2000; Lin et al., 2016), hS100A12 (Moroz et al., 2001; Moroz et al., 2003), hS100A15 (Murray et al., 2012) and hS100B (Ostendorp et al., 2007; Ostendorp et al., 2011) homodimers, whether they are Ca^{2+}-bound (hS100A8, hS100A12, hS100B), Ca^{2+}/Zn^{2+}-bound (hS100A7, hS100A8, hS100A15, hS100B) or even Ca^{2+}/Cu^{2+}-bound (hS100A12). In fact, no major repositioning of the two S100 subunits is observed in these different S100 homodimers upon zinc addition to the Ca^{2+}-bound form. This suggests that the differential S100/S100 orientation we observe between Ca^{2+}-bound hS100A9 and Ca^{2+}/Zn^{2+}-bound mS100A9 is not a direct consequence of zinc binding. The fact that the hS100A9 structures have been determined either by NMR (for the WT protein) or by X-ray crystallography but using a hS100A9 mutant form (for the C3S mutant) may also account for the observed differences. In any case, the quaternary organization of our Ca^{2+}/Zn^{2+}-bound mS100A9 homodimer is very similar to that of other Ca^{2+}/Zn^{2+}-bound s100 homodimers.

3.2. mS100A9 harbors two distinct types of zinc binding sites

To our knowledge, no biophysical characterization of zinc binding to the S100A9 homodimer has been published so far, although S100A9 is known to bind zinc in the absence of its S100A8 congener (Bjork et al., 2009). In particular, the stoichiometry of zinc binding to the S100A9 homodimer and the exact nature of the cation binding sites remain unknown. Unexpectedly, our structure of Ca^{2+}/Zn^{2+}-bound mS100A9 revealed the presence of two Zn^{2+} ions per S100A9 protomer. The first binding site is positioned at the interface between the two mS100A9 subunits. The mS100A9 homodimer contains two equivalent sites of this type, arranged centro-symmetrically (Zn1 and Zn3 in Figure 1A) and displaying a tetrahedral geometry (Fig. 2A), with

382 average Zn-ligand bond distances between 1.9 and 2.0 Å (Table 2). The first mS100A9 subunit
383 provides two of the coordinating residues, His21 at the end of helix H1, and Asp31 within the first
384 Ca^{2+} EF-hand. The two other Zn^{2+}-chelating residues, His92 and His96, come from helix H4 in
385 the second subunit. This site corresponds to the canonical His_3Asp zinc binding motif which is
386 encountered in the His-Zn class of S100 proteins, and its geometry is highly similar to that of the
387 His-Zn sites present in hS100A7 (Brodersen et al., 1999; Supplementary Fig. S3A) and hS100A12
388 (Moroz et al., 2009a; Supplementary Fig. S3B). The geometry of this site also corresponds well to
389 that of the Zn-binding sites found in hS100B (Ostendorp et al., 2011; Supplementary Figure S3C)
390 and hS100A8 (Lin et al., 2016; Supplementary Figure S3D), although in these two cases the
391 coordinating motifs are respectively His_3Glu and His_4.

392 The second Zn-binding site observed in our structure involves the three histidine residues located
393 in the C-terminal tail of mS100A9 (Fig. 2B, purple triangles). These three C-terminal His residues
394 form a novel, tetrahedral Zn^{2+}-binding motif (Fig. 2C), never encountered so far in other S100
395 protein structures. The fourth coordinating residue, Glu65 at the end of helix H3, is provided by a
396 symmetry-related mS100A9 molecule within the crystal. Average Zn-ligand bond distances for
397 this second Zn-site range between 1.9 and 2.1 Å (Table 2). Due to the involvement of its three His
398 residues in zinc chelation, the C-terminal tail folds back over the mS100A9 subunit core. This
399 folding is further promoted by the presence of a disulfide bridge connecting Cys91, at the end of
400 helix H4, and Cys111 at the end of the C-terminal tail. The C-terminal tail therefore adopts a
401 rigidified architecture, forming a closed loop that protrudes at the extremity of helix H4 (Fig. 2D).
402 This novel Zn-binding site is rendered possible in mS100A9, at least in the crystal structure,
403 because the three His residues in its C-terminal portion are not placed contiguously but are instead
404 spaced by a residue of different nature, giving rise to an HxHxH motif (Fig. 2B). hS100A9 likewise

contains a cluster of histidine residues in its C-terminal tail (Fig. 2B, orange circles). Since no structure of the hS100A9 homodimer bound to zinc is available, it is not possible to know if such a site can be formed within the human homodimer. However, the structures of the human S100A8/A9 heterocomplex bound to Mn^{2+} or Ni^{2+} (Damo et al., 2013; Nakashige et al., 2018) revealed that in hS100A9, these C-terminal His residues participate in the coordination of the Mn^{2+} ion present at the interface between the two S100 subunits, thereby generating an octahedral His_6 coordination site with high affinity. In the context of the S100A8/A9 heterocomplex, this non-canonical His_6 site was shown to bind both Zn^{2+}, Mn^{2+}, Ni^{2+} and Fe^{2+} (Damo et al., 2013; Nakashige et al., 2015; Nakashige et al., 2017). It remains unknown whether such an octahedral site would also be used for zinc chelation in the context of the hS100A9 homodimer or whether hS100A9 could also form a second Zn-binding site, similar to the one we observe for mS100A9. Obviously, since the three terminal histidines of hS100A9 are contiguous to each other (Fig. 2B), the geometrical constraint imposed on the protein backbone would only allow two of them to arrange simultaneously in a tetrahedral coordination motif, and the two remaining Zn-ligand would have to be provided by a distinct molecule/ion.

Since the novel Zn-site we observe in mS100A9 structure is promoted by crystal contacts, we investigated whether it was a crystallization artifact or whether it could also exist in solution. For this purpose, we first confirmed that our mS100A9 sample had been purified in the apo form by quantifying the residual content of divalent cations present in our protein preparation using inductively-coupled plasma mass spectrometry (ICP-MS). The measured metal/S100 ratios show that there is no significant metal-ion contamination in our sample (Table 3). We then performed ITC titrations of zinc binding to mS100A9, either in the absence or presence of calcium. As shown in Figures 3A and 3B, the thermograms were best fitted with a single-site model, indicating that

mS100A9 binds one Zn^{2+} ion per subunit with an average dissociation constant (K_d) ranging between 16 and 25 μM depending on the experiments. Thus, the mS100A9 homodimer possesses two equivalents Zn-binding sites with affinities in the medium μM range. Differences in K_d values between apo mS100A9 and Ca^{2+}-bound mS100A9 are within error range, suggesting that calcium has no effect on mS100A9 affinity for zinc. A few of the titrations curves exhibited a small, second phase that could indicate a biphasic binding mode but fitting with a two-sites model did not yield pertinent results in these cases (data not shown). Thus, even if a second Zn-binding site exists on the mS100A9 protomer in solution, we could not detect it with the experimental conditions employed here. Importantly, all titrations ended up at 2 molar equivalents of zinc as compared to mS100A9. When we increased further zinc concentration in the titrations, mS100A9 started precipitating. To analyze this metal-dependent aggregation of mS100A9 in more details, we performed DLS analysis of the sample, both in the presence and absence of calcium, using increasing concentrations of zinc. As depicted in Figures 3C and 3D, zinc-dependent aggregation of mS100A9 readily occurs as soon as the zinc to mS100A9 molar ratio equals or exceeds 3 equivalents and this phenomenon is independent of calcium. This tendency to aggregate in the presence of excess zinc evidently complicates the analysis of the Zn-mS100A9 samples with native MS (see below). It may also impair the detection of low affinity Zn-binding sites by ITC.

3.3. In solution, mS100A9 exists as several homodimeric forms with distinct disulfide bond patterns

Our structure reveals that mS100A9 forms an intramolecular disulfide bridge between Cys91 and Cys111, at least in the presence of high calcium and zinc concentrations. By contrast, a disulfide bridge between Cys80 and Cys91 was previously reported for the protein isolated from native source or produced recombinantly in the absence of divalent cations (Raftery et al., 1999).

Presence of divalent cations may therefore influence SS link formation within mS100A9. In particular, zinc coordination at the C-terminal tail may preferentially stabilize the Cys91-Cys111 SS bridge (or *vice versa*). To gain more insight into the disulfide bonding pattern of wild-type (WT) mS100A9, we analyzed the dimeric pool of mS100A9 under denaturing conditions using LC/ESI-TOF MS (Supplementary Fig. S4). This technique enables the characterization of both inter- and intramolecular disulfide crosslinks whereas all the non-covalent interactions are broken (Boeri Erba et al., 2018).

We first analyzed WT mS100A9 in the absence of divalent cations. When all three cysteines are reduced (i.e. are not engaged in an SS-bond), our mS100A9 protein has a theoretical mass of 13177.1 Da as a monomer, and of 26354.2 Da as a homodimer. Under denaturing conditions and in the absence of DTT, WT mS100A9 generates an LC/ESI-TOF MS spectrum with one major peak (Fig. 4A; mass 13175.1 Da, 66% of the total protein signal) referred to as the "monomeric" peak and whose mass confirms the presence of one intramolecular disulfide bond per molecule. Since the mS100A9 sample was analyzed under denaturing conditions, the "monomeric" peak is composed of both native monomers and single subunits generated by the disassembly of non-covalent oligomers. The ESI MS spectrum also reveals a minor peak (Fig. 4A; mass 26349.5 Da, 34% of the total protein signal) referred to as the "dimeric" peak. Upon reduction with DTT, the "dimeric" peak almost totally disappears (Fig. 4D), confirming that the mS100A9 form(s) giving rise to this peak contain intersubunit disulfide bonds.

To characterize the oligomeric state of these covalent and non-covalent forms of mS100A9, we analyzed the same samples using native MS. In both absence and presence of DTT, mS100A9 is mostly dimeric (Figs. 4B-C; mass: 26351 ± 2 Da and 26355 ± 3 Da, respectively), in agreement with our SEC experiments (Supplementary Fig. S1B). A small amount of monomer is also

observed in both conditions (Figs. 4B-C; mass: 13175 ± 2 Da and 13177 ± 1 Da, respectively). Due to the gentle experimental conditions employed, native MS is a technique that preserves non-covalent interactions (Boeri Erba et al., 2020). The monomeric state we observe can therefore not arise from the breaking of dimers during data acquisition. Interestingly, mS100A9 carries less charges in the presence of disulfide bridges (Figs. 4B-C). This reflects the higher degree of compactness of the disulfide crosslinked mS100A9 compared to the non-crosslinked one. This is also in agreement with our SEC experiments which show that in the presence of DTT, the peak corresponding to homodimeric mS100A9 elutes slightly earlier than under non-reducing conditions (Supplementary Fig. S1B), suggesting a less compact form in the presence of DTT. Addition of DTT does not yield a significantly higher proportion of monomeric mS100A9 (Fig. 4C), suggesting that mS100A9 remains dimeric upon breakage of the intersubunit SS bridges.

To assess the number of free cysteines, we treated mS100A9 with iodoacetamide (IAA), in the absence or presence of DTT, and we analyzed these samples using LC/ESI-TOF MS (Figs. 4E-F). Reaction with IAA increases the mass of the "monomeric" peak to 13232.1 Da (+ 57 Da), indicating the covalent addition of one acetamide group per molecule (Figs. 4E, 4G). This suggests that only one cysteine per mS100A9 molecule is free to react with IAA. Treatment with DTT and IAA gives rise mainly to addition of 1 and 2 acetamide groups (Figs. 4F-G). Thus, DTT reduces two cysteines that were previously engaged in an intramolecular disulfide bridge. Species with 3 acetamide groups were not detected after DTT and IAA treatment. There are several explanations: one of the three cysteines may be partly inaccessible to the solvent after cleavage of the SS bridge; alternatively, the reaction conditions may not be sufficient to reduce all cysteines. To address this question, we incubated mS100A9 with DTT in the presence of strong denaturant (8M urea) before performing alkylation with IAA using identical conditions as previously. In these conditions, we

obtained fully tri-alkylated protein (Fig. 4H, species at molecular mass 13348.3 Da). Thus, upon complete unfolding of the protein, all three cysteines reacted with IAA.

Reaction with IAA increases the mass of the "dimeric" peak of 114 Da, indicating a covalent addition of 2 acetamide groups per dimer (Figs. 4E, 4I). This means that only two cysteines (out of six available) are free to react. We may hypothesize two intersubunit SS bonds between two S100A9 protomers, forming a covalent dimer. Another possibility is that only one inter-subunit SS bond bridges the two mS100A9 protomers and one of the protomers also bears an intramolecular SS bridge.

Altogether MS data suggest that 1) WT mS100A9 forms both non-covalent and SS-crosslinked homodimers (Figs. 4A-4D); 2) the protein also exists as a monomer (Figs. 4B-C); 3) the non-covalent species all contain one intramolecular disulfide bridge per S100A9 subunit (Fig. 4G).

3.4. The homodimerization mode of mS100A9 is differentially affected by calcium and zinc

Next, we aimed to investigate the effect of divalent cations on the mS100A9 dimeric pool. Thus, we performed LC/ESI-TOF and native MS experiments on WT mS100A9 incubated in the presence of calcium alone, zinc alone, or both metals (Supplementary Fig. S4). As shown in Figure 5, we observe the presence of both the "monomeric" and "dimeric" peaks in the LC/ESI-TOF spectra regardless of the metal present. However, when zinc is present, the equilibrium is significantly shifted towards the formation of SS-crosslinked homodimers (Figs. 5C, 5E).

In the absence of divalent cations or in the sole presence of calcium, the "monomeric" peak observed under denaturing conditions is predominant (Figs. 4A, 5A). In the native MS conditions, the non-covalent homodimer is in equilibrium with a monomeric form of the protein, whose abundance remains low (Fig. 4B, 5B). The use of IAA shows that calcium does not affect the disulfide bond pattern of the non-covalent and SS-crosslinked homodimers (Supplementary Fig.

S5). In the presence of calcium, the "monomeric peak" still contains an intramolecular SS bridge per subunit (Supplementary Figs. S5A-C), whereas the disulfide-crosslinked homodimer has two SS bonds and two free cysteines (Supplementary Fig. S5D). The addition of calcium seems only to loosen slightly the monomer packing in the homodimer as illustrated by the observed shift to higher charge states in the native MS spectrum (Fig. 5B).

Regardless of whether calcium is bound or not, the presence of zinc highly affects mS100A9 behavior. The disulfide-crosslinked homodimer becomes predominant, representing 86 % and 80 % of the total amount of protein in the presence of zinc alone or zinc and calcium, respectively (Figs. 5C, 5E). The observed molecular mass of this "dimeric" peak increases of +2 Da, suggesting that one of the two SS bridges is lost. Interestingly, native MS shows that the signals of mS100A9 monomers are not observed anymore (Figs. 5D, 5F). Moreover, it was quite difficult to record native MS data when zinc was present since the sample tended to aggregate during injection into the mass spectrometer. Thus, as also suggested by our DLS experiments, zinc may promote the formation of high order insoluble oligomers and the recorded spectra may only reflect the soluble fraction of the sample.

In the sample with zinc alone, reaction with IAA generates species carrying one acetamide group for the "monomeric" peak (Supplementary Fig. S6A). Pre-treatment with DTT yields species carrying up to 2 acetamide groups (Supplementary Figs. S6B-C). The binding of 3 acetamide groups is not observed, indicating that a maximum of two cysteines per molecule is available. Zinc might hinder solvent accessibility of the third cysteine either because Zn^{2+}-binding sites may directly block the access to this residue or because zinc may promote mS100A9 oligomerization, thereby diminishing solvent exposure of the cysteines buried within the oligomers. Surprisingly, in the presence of both calcium and zinc, no alkylation of the non-covalent species occurs

(Supplementary Fig. S7A). Similarly, addition of DTT and IAA leads mainly to the formation of species with 1 acetamide group, and a smaller amount of species with 2 acetamide groups, as well as a certain amount of unreacted protein (Supplementary Figs. S7B-C).

Up to four acetamide groups are bound to the disulfide-crosslinked homodimer in the presence of zinc alone (Supplementary Fig. S6D), whereas only two acetamide groups are added in the sole presence of calcium (Supplementary Fig. S5D). This demonstrates loss of one SS bridge upon zinc addition. When calcium and zinc are present, the SS-linked homodimer is almost unreactive towards alkylation, the major form observed is the unreacted protein, whose mass corresponds to a dimer carrying one intersubunit SS bridge (Supplementary Fig. S7D). Small amounts of homodimers with 1 and 2 acetamide groups are also detected but clearly the cysteines are much less accessible to IAA when both cations are present. Taken together, these data suggest that zinc act as a modulator of the disulfide bonding pattern of mS100A9. It promotes the assembly of covalent, SS-crosslinked dimers and affects the accessibility of the other unliganded cysteines.

3.5. The formation of distinct SS bridges allows switching between the different homodimeric forms of mS100A9

In order to identify which of the three cysteines of mS100A9 are involved in the intramolecular and inter-subunit disulfide bridges, point mutations into alanine were introduced for each cysteine residue. Only the dimeric fraction of the samples was pooled from the SEC column (Supplementary Fig. S8). These dimeric pools were first analyzed by SDS-PAGE under non-reducing conditions for all four ionic conditions tested. As shown in Figure 6A, regardless of the metal present, almost no disulfide-crosslinked dimer is observed for the C111A mutant, whereas the C91A mutant forms almost exclusively the disulfide-crosslinked dimers. For both the WT protein and the C80A mutant, a mixture of monomers and SS-linked dimers is present. The relative

proportion of monomers and dimers is however difficult to evaluate and it is apparently not highly influenced by cations (Figure 6A).

In order to assess the mass of the species with high accuracy and sensitivity, the three Cys-to-Ala mutants were analyzed by LC/ESI-TOF-MS. C111A mutant is unable to form the disulfide-crosslinked homodimer, regardless of the cations present (Figure 6B), in agreement with our SDS-PAGE experiments. This indicates that Cys111 is responsible for the formation of inter-subunit SS bridge(s). In all four ionic conditions, the "monomeric" peak has an experimental molecular mass of 13145.2 Da. This mass indicates that the two non-mutated cysteines, Cys80 and Cys91, are in the reduced state, regardless of the presence or absence of metal ions. Consistently, treatment of the protein with IAA leads to the binding of two acetamide groups per subunit, when there is Ca only, Zn only or no metal (Supplementary Fig. S10A). When both zinc and calcium are present, one cysteine is less accessible to react with IAA. These data rule out the formation of an intramolecular bridge between Cys80 and Cys91, and suggest that Cys111 also participates in the intramolecular SS links. Alternatively, Cys111 mutation into alanine may affect the overall architecture of the S100A9 molecule in such a way that the SS bridge between Cys80 and Cys91 cannot be formed. As Cys111 is located at the very end of mS100A9 C-terminal tail, in a highly flexible and unstructured region, it seems however unlikely that the C111A mutation may modify significantly the architecture of the protein core.

By contrast, the C91A mutant is exclusively present as disulfide-crosslinked dimers, in all ionic conditions screened (Fig. 6C). The measured molecular mass indicates a homodimer containing one inter-subunit SS bond and two reduced cysteines. Consistently, reaction with IAA leads mainly to the addition of 2 acetamide groups, except when both zinc and calcium are present. In that case, the protein is mostly present in its non-alkylated form (Supplementary Fig. S10B). These

observations suggest that Cys91 is not essential to the formation of the SS-linked homodimer and that Cys91 mutation frees two cysteines by removing one of the SS bonds present within the disulfide-crosslinked dimer.

In the case of the C80A mutant, different forms of mS100A9 are in equilibrium (Fig. 6D). In the absence of metals or in the presence of zinc, the disulfide-crosslinked homodimer represents the most abundant form of the protein whereas non-covalent species are slightly prevailing in the presence of calcium alone. The "monomeric" peak has a molecular mass consistent with one intramolecular SS bridge per mS100A9 subunit (Fig. 6D). Moreover, reaction with IAA does not result in alkylation of the protein, demonstrating that the two non-mutated cysteines, Cys 91 and Cys111, are not available to react due to their engagement in the intramolecular SS link (Supplementary Fig. S10C). The disulfide-crosslinked homodimer displays a mass indicating the presence of a single inter-subunit SS bridge and two reduced cysteines. These residues are available for alkylation by IAA, when there is calcium or zinc or no metals (Supplementary Fig. S10D). When both zinc and calcium are present, the unreacted protein represents the major species. This may be explained by oligomerization and/or local conformational changes hindering access to free cysteines.

In a further effort to unravel how the three cysteines interact with each other, in particular within the disulfide-crosslinked homodimer, we aimed to crystallize the three Cys-to-Ala mS100A9 point mutants in the various ionic conditions screened. We managed to obtain crystals for the mS100A9 C80A mutant, in the presence of calcium and zinc, in the same crystallization conditions than for the WT protein. These crystals diffracted X-rays to 2.35 Å resolution (Table 1, Supplementary Table S2). The structure of the Ca^{2+}/Zn^{2+}-bound point mutant was determined by MR using the structure of the WT protein obtained in this study. The resulting structural model is reported in

Figure 7A and the quality of the fit with the electron density map is depicted in Supplementary Figure S11A. The overall structure of the mutant is highly similar to the structure of the WT protein, with an r.m.s.d. value on Cα atoms of 0.2 Å between the two structures (Fig. 7A). As for the WT protein, the C80A mutant forms a non-covalent homodimer with two calcium and two zinc bound per protomer and one intramolecular SS bridge connecting Cys91 and Cys111 (Fig. 7A, Supplementary Fig. 11B). This second structure confirms that within the non-covalent species, Cys80 is not involved in the formation of intramolecular SS bonds.

In summary, our results indicate that Cys91 and Cys111 are able to form an intramolecular SS bridge in the absence or presence of calcium and/or zinc. Characterization of the SS inter-subunit bridges in the disulfide-crosslinked dimer is more complex. The dimer strongly relies on Cys111, whether metals are present or not. It contains two SS bridges, one of which is lost upon addition of zinc as well as when Cys80 or Cys91 are point-mutated. There may not be a single SS-linked homodimeric form of mS100A9 and the protein may display quite some flexibility in the way its subunits are connected through disulfide bridges.

4. Discussion

In this study, we provided a detailed *in vitro* investigation of the homodimerization and disulfide bond pattern of murine S100A9 and we examined how divalent cations affect these properties. We described the first crystallographic structures of mS100A9 (WT and C80A mutant) obtained in the presence of calcium and zinc. They revealed a canonical architecture for the mS100A9 homodimer, with both protomers arranged in a centro-symmetrical fashion, as observed for most other S100 proteins. The structures also suggested that mS100A9 is able to chelate two zinc ions per subunit, in contrast to what has been reported so far for other members of the family. Indeed, besides the canonical His_3Asp Zn-motif, our structural data uncovered a second, His_3Glu

tetrahedral Zn^{2+}-binding site formed by the HxHxH motif within mS100A9 C-terminal tail and a glutamate side chain coming from a symmetry-related molecule in the protein crystal. This second type of metal-binding site has not been observed in the structures of Mn^{2+}- or Ni^{2+}-bound human S100A8/A9 (Damo et al., 2013; Gagnon et al., 2015; Nakashige et al., 2017; Nakashige et al., 2018). Moreover, it has been proposed that S100A8/A9 also uses the octahedral His_6 site to chelate zinc (Nakashige et al., 2016).

The accurate mechanism and stoichiometry of zinc chelation by the S100A9 homodimer has not been characterized yet. It was reported that a truncated version of mS100A9 encompassing only the first 102 residues (i.e. lacking the three His residues from the C-terminal tail), binds substantially less zinc than the WT protein (Raftery et al., 1999). More recently, Harms and coworkers proposed a biphasic zinc binding mode for the hS100A9 homodimer (unpublished results). In their model, both the His20/Asp30/His91/His95 tetrad and the C-terminal histidines may contribute to zinc chelation, possibly through two distinct binding sites (Loes et al., 2019). These data are consistent with our structural observations of two independent Zn-sites per mS100A9 protomer but they still require confirmation. On the other hand, our ITC experiments (Figs. 3A-B) suggest that in solution, only one zinc ion is bound per mS100A9 subunit, with an affinity much lower than that reported for human calprotectin (Kehl-Fie et al., 2011; Brophy et al., 2012). If the affinity of the second Zn-site is even lower or if the binding is entropy driven, we may not detect it by ITC. In conclusion, we cannot evidence the existence of a second Zn-binding site per mS100A9 protomer in solution, but our structural data still highlight that such a site is geometrically possible. Whether this site is a crystallization artifact or whether it can be formed *in vivo* remains to be determined. This Zn-site may not exist in the context of the sole mS100A9 homodimer, especially knowing that one of the coordinating residues would be missing. It could

for example be pertinent for mS100A9 interaction with specific binding partners, in particular those whose interaction has been described as zinc-dependent (Bjork et al., 2009).

The non-covalent mS100A9 homodimers we observe both in our crystal structure and in solution, through MS analysis, all contain an intramolecular bridge in each S100A9 subunit, between Cys91 and Cys111. This finding correlates with older reports mentioning an intramolecular SS bridge in the protein (Raftery et al., 1998). It remains however uncertain whether all these non-covalent forms display a canonical S100A9/S100A9 arrangement, as reported in our crystallographic models. Remarkably, the Cys91-Cys111 bond leads the otherwise flexible C-terminal tail to adopt a rigidified architecture by folding back over the tip of helix H4. This mechanism seems to be zinc-independent since the disulfide bond pattern of the non-covalent homodimers is not affected by divalent cations. As a consequence, mS100A9 C-terminal tail adopts a conformation unique to the murine protein, regardless of the ions present. Behaviourial differences between murine and human S100 proteins have been described for several members of the family, including S100A8 (Lackmann et al., 1993; Lim et al., 2009). This is also the case for S100A9: hS100A9 is generally considered as pro-inflammatory, especially in a cancer context (Gebhardt et al., 2006), whereas mS100A9 may rather display anti-inflammatory properties (Dale et al., 2006; Otsuka et al., 2009; Gomes et al., 2013; Wang et al., 2018b). These latter properties were attributed to mS100A9 C-terminal tail, which can inhibit hyperalgesia by modulating calcium channel signaling in sensory neurons (Dale et al., 2009). However, the mS100A9 C-terminal peptide used in these studies lacked both cysteines involved in the intramolecular SS-bridge. Consequently, it would not adopt the hairpin-like 3D-fold we observe in our structures. Modulation of the 3D-architecture of S100A9 C-terminal tail should therefore be taken into account when designing peptides with more potent antinociceptive effects. Furthermore, the unique architecture of mS100A9 C-terminal tail

should be kept in mind when comparing the physiological properties of hS100A9 and mS100A9. While the interconversion between pro- and anti-inflammatory functions for S100A9 is possibly influenced by both the pathological and the cell contexts, differential properties observed between human and murine S100A9 may also be inherent to their distinct 3D-architectures, especially in their C-terminal region known to be critical for effector binding.

Formation of disulfide-crosslinked S100A9 homodimers has already been described in the literature (Shibata et al., 2004). Our MS data provide novel insights into these disulfide-crosslinked species and how divalent cations may influence their formation. Indeed, we observed that the SS-linked homodimers bear one inter-subunit disulfide bridge, which strongly relies on Cys111, and a second SS bond, either inter- or intramolecular, which is lost when zinc is added or when Cys80 or Cys91 are mutated. It is not straightforward to reconcile all these observations in a single model. The Cys111-Cys111 interaction is the sole inter-subunit SS bridge consistent with a canonical S100A9 homodimer (Fig. 7B). Other inter-subunit interactions would require a substantial repositioning of the two S100A9 protomers with respect to each other and/or conformational changes within each protomer. Other models for which the S100A9/S100A9 arrangement differs dramatically from the canonical configuration we observe in our crystal structures may also help describe these SS-linked homodimers. For example, some of these forms may adopt a two-fold symmetrical homodimeric arrangement, similar to the one we observed for S100A6 in complex with the full-length RAGE ectodomain (Yatime et al., 2016). Interestingly, we speculated at that time that the novel S100A6 conformation may be utilized by other S100 proteins, possibly stabilized by inter-subunit SS bond (Yatime et al., 2016; Yatime, 2017). The different SS-crosslinked mS100A9 dimers may also display other yet unraveled quaternary architectures. These models for the disulfide-crosslinked mS100A9 homodimer(s) are still speculative without

structural data. Nevertheless, our results clearly indicate that mS100A9 adopts multiple homodimeric arrangements that rely on distinct disulfide bond patterns and are modulated by the cations present. Local calcium/zinc concentrations may also influence the respective proportion of these forms, possibly through metal-induced crosslinking/oligomerization.

It becomes more and more evident that not only mS100A9, but also other S100 proteins exist *in vivo* as multiple forms, this plasticity helping understand how these proteins can achieve so many diverse and sometimes opposite functions. Disulfide-crosslinked homodimers have been reported, both *in vitro* and *in vivo*, for many other S100 proteins, including S100A2 (Yamaguchi et al., 2016), S100A4 (Haase-Kohn et al., 2011), S100A5 (Schafer et al., 2000), S100A6 (Wojda et al., 1994), S100A8 (Harrison et al., 1999), S100B (Winningham-Major et al., 1989), and the S100A8/A9 heterodimer (Stephan et al., 2018; Hoskin et al., 2019). None of these forms has been characterized from a structural point of view yet, due to the difficulty of isolating them *in vitro*. Nevertheless, evidence has accumulated suggesting that oxidation may contribute to the modulation of S100 function *in vivo*. In the case of the S100A8/A9 heterocomplex, both intramolecular and inter-subunit disulfide crosslinks have been identified (Stephan et al., 2018; Hoskin et al., 2019). The resulting SS-crosslinked complexes were shown *in vitro* to be more susceptible to protease degradation. This suggests a way to remove unnecessary S100A8/A9 present in the extracellular space and thereby down-tune both the inflammatory and antimicrobial activities of the heterocomplex (Magon et al., 2015; Stephan et al., 2018; Hoskin et al., 2019).

An interplay between metal binding and oxidation-dependent regulation has also been reported for several S100 proteins. For example, disulfide crosslinking of S100A4 in the presence of copper was shown to enhance pro-inflammatory responses in the tumor microenvironment, through increased RAGE signaling (Haase-Kohn et al., 2011). Similarly, SS-linked S100B dimers promote

neuronal growth and proliferation of glial cells (Winningham-Major et al., 1989). S100B crosslinking is also induced by excess copper and may stimulate a toxic response, through nitric oxide production, in relevant neuropathological conditions (Matsui Lee et al., 2000). Cu^{2+}-oxidized forms of S100A1, S100A2, S100A6, S100B and S100P were also described, leading to SS-crosslinked dimers at least for S100A2 (Yamaguchi et al., 2016). These forms were shown to modulate PP5 phosphatase activity, possibly impacting on apoptotic responses to oxidative stress. Copper-mediated oxidation of murine S100A8 also generated SS-crosslinked dimers that lost their chemotactic properties, thereby preventing leukocyte recruitment (Harrison et al., 1999). Conversely, SS bond formation may also regulate S100 metal binding properties. Formation of an intramolecular disulfide bridge within human S100A7 was shown to enhance metal sequestration by the canonical His3Asp Zn-binding site, through allosteric modulation, thereby increasing S100A7 antimicrobial activity (Cunden et al., 2017).

These examples demonstrate how subtle modulations of the 3D/4D-architecture of S100 proteins may dramatically affect their biological properties. Interestingly, reports also start emerging on possible crosslinking between molecules of RAGE, the cognate receptor for several members of the S100 family (Wei et al., 2012; Moysa et al., 2019). All these findings underline the importance of further studying S100 disulfide-crosslinked forms, in order to understand what is their function and which factors/mechanisms promote their formation *in vivo*. The in-depth characterization of these various forms and of their physiological functions will clearly be a prerequisite to propose efficient targeting strategies against S100 proteins in a context where their pro-inflammatory properties become deleterious, while preserving their beneficial functions such as their antimicrobial activity, these antagonistic effects being possibly orchestrated by distinct forms of the proteins.

Accession codes

The structure factors and atomic coordinates for the crystal structures of WT and C80A mS100A9 in the presence of calcium and zinc have been deposited in the Protein Data Bank as entries 6ZDY and 6ZFE, respectively (http://www.wwpdb.org/).

CRediT authorship contribution statement

Luca Signor: Methodology, Investigation, Formal analysis, Visualization, Writing – original draft. Theo Paris: Investigation. Caroline Mas: Methodology, Investigation, Formal analysis, Visualization. Adrien Picard: Investigation. Georges Lutfalla: Funding acquisition. Elisabetta Boeri Erba: Methodology, Investigation, Formal analysis, Resources, Visualization, Writing – original draft. Laure Yatime: Conceptualization, Methodology, Investigation, Formal analysis, Supervision, Resources, Funding acquisition, Visualization, Writing – original draft.

Declaration of Competing Interest

The authors declare that they have no known competing financial interests or personal relationships that could have appeared to influence the work reported in this paper.

Acknowledgements

We thank the beamline staffs at ESRF and SLS for technical assistance. We thank Dr. Mickael Blaise for initial data collection for the WT protein and Dr. Vincent Olieric for help with data collection for the C80A mutant. We are grateful to Rémi Freydier and Léa Causse from the AETE-ISO platform in the Hydrosciences laboratory (Montpellier, France) for their help with the ICP-MS measurements. We thank Dr. Cherine Bechara for fruitful discussion. This work used the platforms of the Grenoble Instruct-ERIC center (ISBG; UMS 3518 CNRS-CEA-UGA-EMBL)

within the Grenoble Partnership for Structural Biology (PSB), supported by FRISBI (ANR-10-INBS-05-02) and GRAL, financed within the University Grenoble Alpes graduate school (Ecoles Universitaires de Recherche) CBH-EUR-GS (ANR-17-EURE-0003). IBS acknowledges integration into the Interdisciplinary Research Institute of Grenoble (IRIG, CEA). Financial support to access the ISBG platform was provided by Instruct-ERIC (PID 6047). We also would like to acknowledge the French Infrastructure for Integrated Structural Biology (FRISBI) for providing access to ESRF and the Danish Cancer Society for initial financial support.

Appendix A. Supplementary data

Supplementary data to this article can be found online.

References

Adams, P.D., Afonine, P.V., Bunkoczi, G., Chen, V.B., Davis, I.W., Echols, N. et al., 2010. PHENIX: a comprehensive Python-based system for macromolecular structure solution. Acta Cryst. D 66, 213-221. https://doi.org/10.1107/S0907444909052925.

Baudier, J., Glasser, N., Gerard, D., 1986. Ions Binding to S100 Proteins .1. Calcium-Binding and Zinc-Binding Properties of Bovine Brain S100-Alpha-Alpha, S100a-(Alpha,Beta), and S100b-(Beta-Beta), Protein - Zn-2+ Regulates Ca-2+ Binding on S100b Protein. J. Biol. Chem. 261, 8192-8203.

Bjork, P., Bjork, A., Vogl, T., Stenstrom, M., Liberg, D., Olsson, A. et al., 2009. Identification of human S100A9 as a novel target for treatment of autoimmune disease via binding to quinoline-3-carboxamides. PLoS Biol 7, e97. https://doi.org/10.1371/journal.pbio.1000097.

Boeri Erba, E., Petosa, C., 2015. The emerging role of native mass spectrometry in characterizing the structure and dynamics of macromolecular complexes. Protein Sci 24, 1176-1192. https://doi.org/10.1002/pro.2661.

Boeri Erba, E., Signor, L., Oliva, M.F., Hans, F., Petosa, C., 2018. Characterizing Intact Macromolecular Complexes Using Native Mass Spectrometry. Methods Mol Biol 1764, 133-151. https://doi.org/10.1007/978-1-4939-7759-8_9.

802 Boeri Erba, E., Signor, L., Petosa, C., 2020. Exploring the structure and dynamics of
803 macromolecular complexes by native mass spectrometry. J Proteomics 222, 103799.
804 https://doi.org/10.1016/j.jprot.2020.103799.

805
806 Brodersen, D.E., Nyborg, J., Kjeldgaard, M., 1999. Zinc-binding site of an S100 protein
807 revealed. Two crystal structures of Ca2+-bound human psoriasin (S100A7) in the Zn2+-loaded
808 and Zn2+-free states. Biochemistry 38, 1695-1704. https://doi.org/10.1021/bi982483d.

809
810 Brophy, M.B., Hayden, J.A., Nolan, E.M., 2012. Calcium ion gradients modulate the zinc
811 affinity and antibacterial activity of human calprotectin. J. Am. Chem. Soc. 134, 18089-18100.
812 https://doi.org/10.1021/ja307974e.

813
814 Chaabouni, T., Manceau, H., Peoc'h, K., 2016. Interest of fecal calprotectine dosage in
815 inflammatory bowel diseases, state of the art and perspectives. Ann Biol Clin (Paris) 74, 385-
816 394. https://doi.org/10.1684/abc.2016.1172.

817
818 Chang, C.C., Khan, I., Tsai, K.L., Li, H., Yang, L.W., Chou, R.H. et al., 2016. Blocking the
819 interaction between S100A9 and RAGE V domain using CHAPS molecule: A novel route to
820 drug development against cell proliferation. Biochim. Biophys. Acta 1864, 1558-1569.
821 https://doi.org/10.1016/j.bbapap.2016.08.008.

822
823 Corbin, B.D., Seeley, E.H., Raab, A., Feldmann, J., Miller, M.R., Torres, V.J. et al., 2008. Metal
824 chelation and inhibition of bacterial growth in tissue abscesses. Science 319, 962-965.
825 https://doi.org/10.1126/science.1152449.

826
827 Cunden, L.S., Brophy, M.B., Rodriguez, G.E., Flaxman, H.A., Nolan, E.M., 2017. Biochemical
828 and Functional Evaluation of the Intramolecular Disulfide Bonds in the Zinc-Chelating
829 Antimicrobial Protein Human S100A7 (Psoriasin). Biochemistry 56, 5726-5738.
830 https://doi.org/10.1021/acs.biochem.7b00781.

831
832 Dale, C.S., Altier, C., Cenac, N., Giorgi, R., Juliano, M.A., Juliano, L. et al., 2009. Analgesic
833 properties of S100A9 C-terminal domain: a mechanism dependent on calcium channel inhibition.
834 Fundam Clin Pharmacol 23, 427-438. https://doi.org/10.1111/j.1472-8206.2009.00686.x.

835
836 Dale, C.S., Pagano Rde, L., Paccola, C.C., Pinotti-Guirao, T., Juliano, M.A., Juliano, L. et al.,
837 2006. Effect of the C-terminus of murine S100A9 protein on experimental nociception. Peptides
838 27, 2794-2802. https://doi.org/10.1016/j.peptides.2006.07.002.

839
840 Damo, S.M., Kehl-Fie, T.E., Sugitani, N., Holt, M.E., Rathi, S., Murphy, W.J. et al., 2013.
841 Molecular basis for manganese sequestration by calprotectin and roles in the innate immune

response to invading bacterial pathogens. Proc. Natl. Acad. Sci. U. S. A. 110, 3841-3846. https://doi.org/10.1073/pnas.1220341110.

Davis, I.W., Leaver-Fay, A., Chen, V.B., Block, J.N., Kapral, G.J., Wang, X. et al., 2007. MolProbity: all-atom contacts and structure validation for proteins and nucleic acids. Nucleic Acids Res. 35, W375-383. https://doi.org/10.1093/nar/gkm216.

Donato, R., Cannon, B.R., Sorci, G., Riuzzi, F., Hsu, K., Weber, D.J. et al., 2013. Functions of S100 proteins. Curr. Mol. Med. 13, 24-57.

Emsley, P., Cowtan, K., 2004. Coot: model-building tools for molecular graphics. Acta Cryst. D 60, 2126-2132. https://doi.org/10.1107/S0907444904019158.

Gagnon, D.M., Brophy, M.B., Bowman, S.E.J., Stich, T.A., Drennan, C.L., Britt, R.D. et al., 2015. Manganese Binding Properties of Human Calprotectin under Conditions of High and Low Calcium: X-ray Crystallographic and Advanced Electron Paramagnetic Resonance Spectroscopic Analysis. J. Am. Chem. Soc. 137, 3004-3016. https://doi.org/10.1021/ja512204s.

Gebhardt, C., Nemeth, J., Angel, P., Hess, J., 2006. S100A8 and S100A9 in inflammation and cancer. Biochem Pharmacol 72, 1622-1631. https://doi.org/10.1016/j.bcp.2006.05.017.

Gilston, B.A., Skaar, E.P., Chazin, W.J., 2016. Binding of transition metals to S100 proteins. Sci China Life Sci 59, 792-801. https://doi.org/10.1007/s11427-016-5088-4.

Giudice, V., Wu, Z., Kajigaya, S., Fernandez Ibanez, M.D.P., Rios, O., Cheung, F. et al., 2019. Circulating S100A8 and S100A9 protein levels in plasma of patients with acquired aplastic anemia and myelodysplastic syndromes. Cytokine 113, 462-465. https://doi.org/10.1016/j.cyto.2018.06.025.

Glaser, R., Harder, J., Lange, H., Bartels, J., Christophers, E., Schroder, J.M., 2005. Antimicrobial psoriasin (S100A7) protects human skin from Escherichia coli infection. Nat Immunol 6, 57-64. https://doi.org/10.1038/ni1142.

Goebeler, M., Roth, J., van den Bos, C., Ader, G., Sorg, C., 1995. Increase of calcium levels in epithelial cells induces translocation of calcium-binding proteins migration inhibitory factor-related protein 8 (MRP8) and MRP14 to keratin intermediate filaments. Biochem J 309 (Pt 2), 419-424.

Gomes, L.H., Raftery, M.J., Yan, W.X., Goyette, J.D., Thomas, P.S., Geczy, C.L., 2013. S100A8 and S100A9-oxidant scavengers in inflammation. Free Radic Biol Med 58, 170-186. https://doi.org/10.1016/j.freeradbiomed.2012.12.012.

Gonzalez, L.L., Garrie, K., Turner, M.D., 2020. Role of S100 proteins in health and disease. Biochim. Biophys. Acta Mol. Cell Res. 1867, 118677. https://doi.org/10.1016/j.bbamcr.2020.118677.

Haase-Kohn, C., Wolf, S., Lenk, J., Pietzsch, J., 2011. Copper-mediated cross-linking of S100A4, but not of S100A2, results in proinflammatory effects in melanoma cells. Biochem. Biophys. Res. Commun. 413, 494-498. https://doi.org/10.1016/j.bbrc.2011.08.132.

Harrison, C.A., Raftery, M.J., Walsh, J., Alewood, P., Iismaa, S.E., Thliveris, S. et al., 1999. Oxidation regulates the inflammatory properties of the murine S100 protein S100A8. J. Biol. Chem. 274, 8561-8569.

Hoskin, T.S., Crowther, J.M., Cheung, J., Epton, M.J., Sly, P.D., Elder, P.A. et al., 2019. Oxidative cross-linking of calprotectin occurs in vivo, altering its structure and susceptibility to proteolysis. Redox Biology 24https://doi.org/Artn 101202

10.1016/J.Redox.2019.101202.

Hunter, M.J., Chazin, W.J., 1998. High level expression and dimer characterization of the S100 EF-hand proteins, migration inhibitory factor-related proteins 8 and 14. J. Biol. Chem. 273, 12427-12435. https://doi.org/10.1074/jbc.273.20.12427.

Ishikawa, K., Nakagawa, A., Tanaka, I., Suzuki, M., Nishihira, J., 2000. The structure of human MRP8, a member of the S100 calcium-binding protein family, by MAD phasing at 1.9 A resolution. Acta Cryst. D 56, 559-566.

Itou, H., Yao, M., Fujita, I., Watanabe, N., Suzuki, M., Nishihira, J. et al., 2002. The crystal structure of human MRP14 (S100A9), a Ca(2+)-dependent regulator protein in inflammatory process. J. Mol. Biol. 316, 265-276. https://doi.org/10.1006/jmbi.2001.5340.

Kabsch, W., 2010. Xds. Acta Cryst. D 66, 125-132. https://doi.org/10.1107/S0907444909047337.

Kallberg, E., Tahvili, S., Ivars, F., Leanderson, T., 2018. Induction of S100A9 homodimer formation in vivo. Biochem. Biophys. Res. Commun. 500, 564-568. https://doi.org/10.1016/j.bbrc.2018.04.086.

Kehl-Fie, T.E., Chitayat, S., Hood, M.I., Damo, S., Restrepo, N., Garcia, C. et al., 2011. Nutrient Metal Sequestration by Calprotectin Inhibits Bacterial Superoxide Defense, Enhancing Neutrophil Killing of Staphylococcus aureus. Cell Host Microbe 10, 158-164. https://doi.org/10.1016/j.chom.2011.07.004.

Kerkhoff, C., Nacken, W., Benedyk, M., Dagher, M.C., Sopalla, C., Doussiere, J., 2005. The arachidonic acid-binding protein S100A8/A9 promotes NADPH oxidase activation by interaction with p67phox and Rac-2. FASEB J. 19, 467-469. https://doi.org/10.1096/fj.04-2377fje.

Korndorfer, I.P., Brueckner, F., Skerra, A., 2007. The crystal structure of the human (S100A8/S100A9)2 heterotetramer, calprotectin, illustrates how conformational changes of interacting alpha-helices can determine specific association of two EF-hand proteins. J. Mol. Biol. 370, 887-898. https://doi.org/10.1016/j.jmb.2007.04.065.

Kraemer, A.M., Saraiva, L.R., Korsching, S.I., 2008. Structural and functional diversification in the teleost S100 family of calcium-binding proteins. BMC Evol Biol 8, 48. https://doi.org/10.1186/1471-2148-8-48.

Lackmann, M., Rajasekariah, P., Iismaa, S.E., Jones, G., Cornish, C.J., Hu, S. et al., 1993. Identification of a chemotactic domain of the pro-inflammatory S100 protein CP-10. J Immunol 150, 2981-2991.

Lagasse, E., Weissman, I.L., 1992. Mouse MRP8 and MRP14, two intracellular calcium-binding proteins associated with the development of the myeloid lineage. Blood 79, 1907-1915.

Leclerc, E., Heizmann, C.W., 2011. The importance of Ca2+/Zn2+ signaling S100 proteins and RAGE in translational medicine. Front Biosci (Schol Ed) 3, 1232-1262. https://doi.org/10.2741/223.

Leukert, N., Vogl, T., Strupat, K., Reichelt, R., Sorg, C., Roth, J., 2006. Calcium-dependent tetramer formation of S100A8 and S100A9 is essential for biological activity. J. Mol. Biol. 359, 961-972. https://doi.org/10.1016/j.jmb.2006.04.009.

Lim, S.Y., Raftery, M.J., Geczy, C.L., 2011. Oxidative modifications of DAMPs suppress inflammation: the case for S100A8 and S100A9. Antioxid Redox Signal 15, 2235-2248. https://doi.org/10.1089/ars.2010.3641.

Lim, S.Y., Raftery, M.J., Goyette, J., Hsu, K., Geczy, C.L., 2009. Oxidative modifications of S100 proteins: functional regulation by redox. J. Leukoc. Biol. 86, 577-587. https://doi.org/10.1189/jlb.1008608.

Lin, H., Andersen, G.R., Yatime, L., 2016. Crystal structure of human S100A8 in complex with zinc and calcium. BMC Struct. Biol. 16, 8. https://doi.org/10.1186/s12900-016-0058-4.

Loes, A.N., Shi, R., Harms, M.J., 2019. Zinc-independent activation of Toll-like receptor 4 by S100A9. bioRxiv, 796219. https://doi.org/10.1101/796219.

Longbottom, D., Sallenave, J.M., van Heyningen, V., 1992. Subunit structure of calgranulins A and B obtained from sputum, plasma, granulocytes and cultured epithelial cells. Biochim. Biophys. Acta 1120, 215-222. https://doi.org/10.1016/0167-4838(92)90273-g.

Ma, L., Sun, P., Zhang, J.C., Zhang, Q., Yao, S.L., 2017. Proinflammatory effects of S100A8/A9 via TLR4 and RAGE signaling pathways in BV-2 microglial cells. Int J Mol Med 40, 31-38. https://doi.org/10.3892/ijmm.2017.2987.

Madeira, F., Park, Y.M., Lee, J., Buso, N., Gur, T., Madhusoodanan, N. et al., 2019. The EMBL-EBI search and sequence analysis tools APIs in 2019. Nucleic Acids Res. 47, W636-W641. https://doi.org/10.1093/nar/gkz268.

Magon, N.J., Turner, R., Gearry, R.B., Hampton, M.B., Sly, P.D., Kettle, A.J., 2015. Oxidation of calprotectin by hypochlorous acid prevents chelation of essential metal ions and allows bacterial growth: Relevance to infections in cystic fibrosis. Free Radic Biol Med 86, 133-144. https://doi.org/10.1016/j.freeradbiomed.2015.05.022.

Marenholz, I., Heizmann, C.W., Fritz, G., 2004. S100 proteins in mouse and man: from evolution to function and pathology (including an update of the nomenclature). Biochem. Biophys. Res. Commun. 322, 1111-1122. https://doi.org/10.1016/j.bbrc.2004.07.096.

Marinkovic, G., Grauen Larsen, H., Yndigegn, T., Szabo, I.A., Mares, R.G., de Camp, L. et al., 2019. Inhibition of pro-inflammatory myeloid cell responses by short-term S100A9 blockade improves cardiac function after myocardial infarction. Eur Heart J 40, 2713-2723. https://doi.org/10.1093/eurheartj/ehz461.

Matsui Lee, I.S., Suzuki, M., Hayashi, N., Hu, J., Van Eldik, L.J., Titani, K. et al., 2000. Copper-dependent formation of disulfide-linked dimer of S100B protein. Arch Biochem Biophys 374, 137-141. https://doi.org/10.1006/abbi.1999.1595.

McCoy, A.J., Grosse-Kunstleve, R.W., Adams, P.D., Winn, M.D., Storoni, L.C., Read, R.J., 2007. Phaser crystallographic software. J. Appl. Crystallogr. 40, 658-674. https://doi.org/10.1107/S0021889807021206.

Morgner, N., Robinson, C.V., 2012. Massign: an assignment strategy for maximizing information from the mass spectra of heterogeneous protein assemblies. Anal Chem 84, 2939-2948. https://doi.org/10.1021/ac300056a.

Moroz, O.V., Antson, A.A., Grist, S.J., Maitland, N.J., Dodson, G.G., Wilson, K.S. et al., 2003. Structure of the human S100A12-copper complex: implications for host-parasite defence. Acta Cryst. D 59, 859-867. https://doi.org/10.1107/s0907444903004700.

Moroz, O.V., Antson, A.A., Murshudov, G.N., Maitland, N.J., Dodson, G.G., Wilson, K.S. et al., 2001. The three-dimensional structure of human S100A12. Acta Cryst. D 57, 20-29. https://doi.org/10.1107/s090744490001458x.

Moroz, O.V., Blagova, E.V., Wilkinson, A.J., Wilson, K.S., Bronstein, I.B., 2009a. The crystal structures of human S100A12 in apo form and in complex with zinc: new insights into S100A12 oligomerisation. J. Mol. Biol. 391, 536-551. https://doi.org/10.1016/j.jmb.2009.06.004.

Moroz, O.V., Burkitt, W., Wittkowski, H., He, W., Ianoul, A., Novitskaya, V. et al., 2009b. Both Ca2+ and Zn2+ are essential for S100A12 protein oligomerization and function. BMC Biochem. 10, 11. https://doi.org/10.1186/1471-2091-10-11.

Moroz, O.V., Wilson, K.S., Bronstein, I.B., 2011. The role of zinc in the S100 proteins: insights from the X-ray structures. Amino Acids 41, 761-772. https://doi.org/10.1007/s00726-010-0540-4.

Moysa, A., Hammerschmid, D., Szczepanowski, R.H., Sobott, F., Dadlez, M., 2019. Enhanced oligomerization of full-length RAGE by synergy of the interaction of its domains. Sci Rep 9, 20332. https://doi.org/10.1038/s41598-019-56993-9.

Murray, J.I., Tonkin, M.L., Whiting, A.L., Peng, F., Farnell, B., Cullen, J.T. et al., 2012. Structural characterization of S100A15 reveals a novel zinc coordination site among S100 proteins and altered surface chemistry with functional implications for receptor binding. BMC Struct. Biol. 12, 16. https://doi.org/10.1186/1472-6807-12-16.

Nacken, W., Sopalla, C., Propper, C., Sorg, C., Kerkhoff, C., 2000. Biochemical characterization of the murine S100A9 (MRP14) protein suggests that it is functionally equivalent to its human

counterpart despite its low degree of sequence homology. European Journal of Biochemistry 267, 560-565. https://doi.org/DOI 10.1046/j.1432-1327.2000.01040.x.

Nakashige, T.G., Bowman, S.E.J., Zygiel, E.M., Drennan, C.L., Nolan, E.M., 2018. Biophysical Examination of the Calcium-Modulated Nickel-Binding Properties of Human Calprotectin Reveals Conformational Change in the EF-Hand Domains and His3Asp Site. Biochemistry 57, 4155-4164. https://doi.org/10.1021/acs.biochem.8b00415.

Nakashige, T.G., Stephan, J.R., Cunden, L.S., Brophy, M.B., Wommack, A.J., Keegan, B.C. et al., 2016. The Hexahistidine Motif of Host-Defense Protein Human Calprotectin Contributes to Zinc Withholding and Its Functional Versatility. J. Am. Chem. Soc. 138, 12243-12251. https://doi.org/10.1021/jacs.6b06845.

Nakashige, T.G., Zhang, B., Krebs, C., Nolan, E.M., 2015. Human calprotectin is an iron-sequestering host-defense protein. Nat. Chem. Biol. 11, 765-771. https://doi.org/10.1038/nchembio.1891.

Nakashige, T.G., Zygiel, E.M., Drennan, C.L., Nolan, E.M., 2017. Nickel Sequestration by the Host-Defense Protein Human Calprotectin. J. Am. Chem. Soc. 139, 8828-8836. https://doi.org/10.1021/jacs.7b01212.

Nakatani, Y., Yamazaki, M., Chazin, W.J., Yui, S., 2005. Regulation of S100A8/A9 (calprotectin) binding to tumor cells by zinc ion and its implication for apoptosis-inducing activity. Mediators Inflamm 2005, 280-292. https://doi.org/10.1155/MI.2005.280.

Ostendorp, T., Diez, J., Heizmann, C.W., Fritz, G., 2011. The crystal structures of human S100B in the zinc- and calcium-loaded state at three pH values reveal zinc ligand swapping. Biochim. Biophys. Acta 1813, 1083-1091. https://doi.org/10.1016/j.bbamcr.2010.10.006.

Ostendorp, T., Leclerc, E., Galichet, A., Koch, M., Demling, N., Weigle, B. et al., 2007. Structural and functional insights into RAGE activation by multimeric S100B. EMBO J 26, 3868-3878. https://doi.org/10.1038/sj.emboj.7601805.

Otsuka, K., Terasaki, F., Ikemoto, M., Fujita, S., Tsukada, B., Katashima, T. et al., 2009. Suppression of inflammation in rat autoimmune myocarditis by S100A8/A9 through modulation of the proinflammatory cytokine network. Eur J Heart Fail 11, 229-237. https://doi.org/10.1093/eurjhf/hfn049.

Paccola, C.C., Gutierrez, V.P., Longo, I., Juliano, L., Juliano, M.A., Giorgi, R., 2008. Antinociceptive effect of the C-terminus of murine S100A9 protein on experimental neuropathic pain. Peptides 29, 1806-1814. https://doi.org/10.1016/j.peptides.2008.05.023.

Pagano, R.L., Moraes, N.F., De Lorenzo, B.H., Coccuzzo Sampaio, S., Mariano, M., Giorgi, R., 2014. Inhibition of macrophage functions by the C-terminus of murine S100A9 is dependent on B-1 cells. Mediators Inflamm 2014, 836491. https://doi.org/10.1155/2014/836491.

Pruenster, M., Vogl, T., Roth, J., Sperandio, M., 2016. S100A8/A9: From basic science to clinical application. Pharmacol Ther 167, 120-131. https://doi.org/10.1016/j.pharmthera.2016.07.015.

Raftery, M.J., Collinson, L., Geczy, C.L., 1999. Overexpression, oxidative refolding, and zinc binding of recombinant forms of the murine S100 protein MRP14 (S100A9). Protein Expr Purif 15, 228-235. https://doi.org/10.1006/prep.1998.1015.

Raftery, M.J., Geczy, C.L., 1998. Identification of posttranslational modifications and cDNA sequencing errors in the rat S100 proteins MRP8 and 14 using electrospray ionization mass spectrometry. Anal Biochem 258, 285-292. https://doi.org/10.1006/abio.1997.2601.

Raftery, M.J., Harrison, C.A., Alewood, P., Jones, A., Geczy, C.L., 1996. Isolation of the murine S100 protein MRP14 (14 kDa migration-inhibitory-factor-related protein) from activated spleen cells: characterization of post-translational modifications and zinc binding. Biochem J 316 (Pt 1), 285-293. https://doi.org/10.1042/bj3160285.

Realegeno, S., Kelly-Scumpia, K.M., Dang, A.T., Lu, J., Teles, R., Liu, P.T. et al., 2016. S100A12 Is Part of the Antimicrobial Network against Mycobacterium leprae in Human Macrophages. PLoS Pathog. 12, e1005705. https://doi.org/10.1371/journal.ppat.1005705.

Reeb, A.N., Li, W., Sewell, W., Marlow, L.A., Tun, H.W., Smallridge, R.C. et al., 2015. S100A8 is a novel therapeutic target for anaplastic thyroid carcinoma. J Clin Endocrinol Metab 100, E232-242. https://doi.org/10.1210/jc.2014-2988.

Roh, J.S., Sohn, D.H., 2018. Damage-Associated Molecular Patterns in Inflammatory Diseases. Immune netw. 18, e27. https://doi.org/10.4110/in.2018.18.e27.

Sakaguchi, M., Yamamoto, M., Miyai, M., Maeda, T., Hiruma, J., Murata, H. et al., 2016. Identification of an S100A8 Receptor Neuroplastin-beta and its Heterodimer Formation with EMMPRIN. J Invest Dermatol 136, 2240-2250. https://doi.org/10.1016/j.jid.2016.06.617.

Schafer, B.W., Fritschy, J.M., Murmann, P., Troxler, H., Durussel, I., Heizmann, C.W. et al., 2000. Brain S100A5 is a novel calcium-, zinc-, and copper ion-binding protein of the EF-hand superfamily. Journal of Biological Chemistry 275, 30623-30630. https://doi.org/DOI 10.1074/jbc.M002260200.

Shabani, F., Farasat, A., Mahdavi, M., Gheibi, N., 2018. Calprotectin (S100A8/S100A9): a key protein between inflammation and cancer. Inflamm Res 67, 801-812. https://doi.org/10.1007/s00011-018-1173-4.

Shibata, F., Miyama, K., Shinoda, F., Mizumoto, J., Takano, K., Nakagawa, H., 2004. Fibroblast growth-stimulating activity of S100A9 (MRP-14). Eur J Biochem 271, 2137-2143. https://doi.org/10.1111/j.1432-1033.2004.04129.x.

Sievers, F., Higgins, D.G., 2018. Clustal Omega for making accurate alignments of many protein sequences. Protein Sci 27, 135-145. https://doi.org/10.1002/pro.3290.

Sobott, F., Hernandez, H., McCammon, M.G., Tito, M.A., Robinson, C.V., 2002. A tandem mass spectrometer for improved transmission and analysis of large macromolecular assemblies. Anal Chem 74, 1402-1407. https://doi.org/10.1021/ac0110552.

Stephan, J.R., Yu, F.T., Costello, R.M., Bleier, B.S., Nolan, E.M., 2018. Oxidative Post-translational Modifications Accelerate Proteolytic Degradation of Calprotectin. J. Am. Chem. Soc. 140, 17444-17455. https://doi.org/10.1021/jacs.8b06354.

Striz, I., Trebichavsky, I., 2004. Calprotectin - a pleiotropic molecule in acute and chronic inflammation. Physiol Res 53, 245-253.

Tomonobu, N., Kinoshita, R., Sakaguchi, M., 2020. S100 Soil Sensor Receptors and Molecular Targeting Therapy Against Them in Cancer Metastasis. Transl Oncol 13, 100753. https://doi.org/10.1016/j.tranon.2020.100753.

Unno, M., Kawasaki, T., Takahara, H., Heizmann, C.W., Kizawa, K., 2011. Refined crystal structures of human Ca(2+)/Zn(2+)-binding S100A3 protein characterized by two disulfide bridges. J. Mol. Biol. 408, 477-490. https://doi.org/10.1016/j.jmb.2011.02.055.

van den Heuvel, R.H., van Duijn, E., Mazon, H., Synowsky, S.A., Lorenzen, K., Versluis, C. et al., 2006. Improving the performance of a quadrupole time-of-flight instrument for macromolecular mass spectrometry. Anal Chem 78, 7473-7483. https://doi.org/10.1021/ac061039a.

Vogl, T., Leukert, N., Barczyk, K., Strupat, K., Roth, J., 2006. Biophysical characterization of S100A8 and S100A9 in the absence and presence of bivalent cations. Biochim. Biophys. Acta 1763, 1298-1306. https://doi.org/10.1016/j.bbamcr.2006.08.028.

Wang, C., Iashchishyn, I.A., Pansieri, J., Nystrom, S., Klementieva, O., Kara, J. et al., 2018a. S100A9-Driven Amyloid-Neuroinflammatory Cascade in Traumatic Brain Injury as a Precursor State for Alzheimer's Disease. Sci Rep 8, 12836. https://doi.org/10.1038/s41598-018-31141-x.

Wang, Q., Chen, W., Lin, J., 2019. The Role of Calprotectin in Rheumatoid Arthritis. J Transl Int Med 7, 126-131. https://doi.org/10.2478/jtim-2019-0026.

Wang, S., Song, R., Wang, Z., Jing, Z., Wang, S., Ma, J., 2018b. S100A8/A9 in Inflammation. Front Immunol 9, 1298. https://doi.org/10.3389/fimmu.2018.01298.

Wei, W., Lampe, L., Park, S., Vangara, B.S., Waldo, G.S., Cabantous, S. et al., 2012. Disulfide bonds within the C2 domain of RAGE play key roles in its dimerization and biogenesis. PLoS One 7, e50736. https://doi.org/10.1371/journal.pone.0050736.

Winningham-Major, F., Staecker, J.L., Barger, S.W., Coats, S., Van Eldik, L.J., 1989. Neurite extension and neuronal survival activities of recombinant S100 beta proteins that differ in the content and position of cysteine residues. J Cell Biol 109, 3063-3071. https://doi.org/10.1083/jcb.109.6.3063.

Wojda, U., Kuznicki, J., 1994. Calcyclin from Mouse Ehrlich Ascites Tumor-Cells and Rabbit Lung Form Noncovalent Dimers. Biochimica Et Biophysica Acta-Protein Structure and Molecular Enzymology 1209, 248-252. https://doi.org/Doi 10.1016/0167-4838(94)90192-9.

Yamaguchi, F., Tsuchiya, M., Shimamoto, S., Fujimoto, T., Tokumitsu, H., Tokuda, M. et al., 2016. Oxidative Stress Impairs the Stimulatory Effect of S100 Proteins on Protein Phosphatase 5 Activity. Tohoku Journal of Experimental Medicine 240, 67-78. https://doi.org/10.1620/tjem.240.67.

Yatime, L., 2017. [A cystein-dependent activation mechanism for the pro-inflammatory ligands of RAGE?]. Med Sci (Paris) 33, 351-354. https://doi.org/10.1051/medsci/20173303026.

Yatime, L., 2019. Structural Analysis of S100A8 Complex with Zinc and Calcium: A General Protocol for the Study of S100 Proteins in the Presence of Divalent Cations by X-Ray Crystallography. Methods Mol Biol 1929, 417-435. https://doi.org/10.1007/978-1-4939-9030-6_26.

Yatime, L., Betzer, C., Jensen, R.K., Mortensen, S., Jensen, P.H., Andersen, G.R., 2016. The Structure of the RAGE:S100A6 Complex Reveals a Unique Mode of Homodimerization for S100 Proteins. Structure 24, 2043-2052. https://doi.org/10.1016/j.str.2016.09.011.

Zackular, J.P., Chazin, W.J., Skaar, E.P., 2015. Nutritional Immunity: S100 Proteins at the Host-Pathogen Interface. J. Biol. Chem. 290, 18991-18998. https://doi.org/10.1074/jbc.R115.645085.

Figure legends

Figure 1. Structure of murine S100A9 in the presence of calcium and zinc. **(A)** General overview of the structure of the Ca^{2+}/Zn^{2+}-bound murine S100A9 (mS100A9) homodimer at 1.45 Å resolution. The two mS100A9 subunits are shown in beige and purple. Calcium and zinc ions are displayed as green and yellow spheres, respectively. **(B)** Final electron density map contoured at 1σ and final model superimposed to assess the quality of the fit. **(C)** Anomalous difference Fourier maps calculated using phases and weight from the best refined atomic model obtained with the native dataset and anomalous differences from the datasets collected at wavelengths of 1.27 Å (blue mesh, contour at 5σ) and 1.30 Å (red mesh, contour at 5σ). The final model displayed as cartoon is superimposed for comparison. **(D)** Superimposition of the mS100A9 protomer from the X-ray structure of Ca^{2+}/Zn^{2+}-bound mS100A9 homodimer (beige, this study) with the hS100A9 moiety from the NMR structure of apo-hS100A9 homodimer (red, PDB_ID 5I8N (Chang et al., 2016)), from the X-ray structure of Ca^{2+}-bound hS100A9 homodimer (cyan, PDB_ID 1IRJ (Itou et al., 2002)) and from the X-ray structure of Ca^{2+}/Mn^{2+}-bound calprotectin heterocomplex (grey, PDB_ID 4GGF (Damo et al., 2013)). Superimposition was performed on C-alpha atoms (mS100A9 residues Glu10 to Leu83). **(E)** Superimposition of the Ca^{2+}/Zn^{2+}-bound mS100A9 homodimer (beige, this study) with apo (red, PDB_ID 5I8N (Chang et al., 2016)) and Ca^{2+}-bound

hS100A9 homodimer (cyan, PDB_ID 1IRJ (Itou et al., 2002)). All 3 homodimers are superimposed on subunit A (superimposition on C-alpha atoms, mS100A9 residues Glu10 to Leu83). **(F)** Superimposition of the Ca^{2+}/Zn^{2+}-bound mS100A9 homodimer (beige, this study) with Ca^{2+}-bound (grey, PDB_ID 1MR8 (Chang et al., 2016)) and Ca^{2+}/Zn^{2+}-bound hS100A8 homodimer (purple, PDB_ID 5HLO (Itou et al., 2002)). All 3 homodimers are superimposed on subunit A (superimposition on C-alpha atoms, mS100A9 residues Glu10 to Leu83).

Figure 2. The two Zn-binding modes of mS100A9: comparison with hS100A9 and influence on the conformation of the C-terminal tail. **(A)** Zoom on the first type of Zn^{2+}-binding site of mS100A9, close to the first Ef-hand motif of subunit A. Anomalous difference Fourier maps calculated using phases and weight from the best refined atomic model (without ions) obtained with the native dataset and anomalous differences from datasets collected at different wavelengths are shown as blue mesh (λ = 1.27 Å, contour at 3.5 σ) or red mesh (λ = 1.30 Å, contour at 3.5 σ). Residues involved in zinc coordination are shown as sticks. (**B**) Sequence alignment of the C-terminal region (Helix H4 + C-terminal tail) of murine and human S100A9. The alignment was performed in Clustal Omega (Sievers et al., 2018; Madeira et al., 2019). The secondary structure is displayed schematically above the alignment. The residue numbering indicated below the alignment corresponds to mS100A9 sequence. Identical residues between the two sequences are underlined in dark green whereas conserved mutations are highlighted in light green. The three cysteines of mS100A9 are indicated with a red star. Histidine residues involved in zinc coordination are marked with orange (Zn-binding site 1) or blue (Zn-binding site 2) triangles for mS100A9 and with orange spheres (Zn-binding site 1) for hS100A9. **(C)** Same as panel **A** but with the close-up view centered on the second type of Zn^{2+}-binding site of mS100A9, within the C-terminal tail of subunit A. (**D**) Overview of the C-terminal region of mS100A9 encompassing helix

H4 and the C-terminal tail closing around the second Zn^{2+} binding site. A disulfide bridge connects Cys91 and Cys111 while Cys80 remains free.

Figure 3. Biophysical investigation of zinc binding to the mS100A9 homodimer. **(A)** ITC titrations and binding isotherms fitted with a one-site model for the binding of Zn^{2+} to apo-mS100A9. Experiments were performed at least in duplicates. The measured K_d value and stoichiometry for each particular experiment are indicated on the graph. **(B)** Same as panel **A** but with Ca^{2+}-bound mS100A9 homodimer. **(C)** DLS analysis of apo-mS100A9 in the presence of increasing concentrations of zinc. Below 3 molar equivalents of zinc, mS100A9 remains homodimeric. At 3 or more equivalents, mS100A9 readily aggregates and forms large oligomers. **(D)** Same as panel **C** but with Ca^{2+}-bound mS100A9.

Figure 4. Mass spectrometry analysis of WT mS100A9 in the absence of divalent cations. **(A)** LC/ESI-TOF-MS deconvoluted spectrum of untreated WT mS100A9. The protein displays two peaks, one at a mass of 13175.1 Da referred to as the "monomeric" peak (M), and one at 26349.5 Da referred to as the "dimeric" peak (D). **(B)** and **(C)** Native MS spectra of WT mS100A9 either untreated (panel B) or after treatment with DTT (panel C) prior to MS analysis. Interestingly, mS100A9 carries less charges in the presence of disulfide bridges. Specifically, the highest peaks of disulfide-bond containing mS100A9 monomeric and dimeric forms are 7+ and 10+, respectively (panel B). On the contrary, the highest peaks of the DTT-treated mS100A9 monomers and dimers are 8+ and 11+, respectively (panel C). These differences in charge reflect the higher degree of compactness of the disulfide cross-linked mS100A9 protein. **(D)**, **(E)** and **(F)** LC/ESI-TOF-MS deconvoluted spectra of WT mS100A9 incubated with either DTT alone (DTT, panel D), iodoacetamide alone (IAA, panel E) or DTT + IAA (panel F) prior to MS analysis. **(G)** Superimposition of the LC/ESI-TOF-MS deconvoluted spectra obtained for WT mS100A9

without any treatment (upper spectrum), incubation with IAA alone (middle spectrum) or with DTT + IAA (lower spectrum). The spectra are centered on the region corresponding to the "monomeric" peak. **(H)** Superimposition of the LC/ESI-TOF-MS deconvoluted spectra obtained for WT mS100A9 without any treatment (upper spectrum) or incubation urea + DTT + IAA (lower spectrum). The spectra are centered on the region corresponding to the "monomeric" peak. **(I)** Superimposition of the LC/ESI-TOF-MS deconvoluted spectra obtained for WT mS100A9 without any treatment (upper spectrum) or after incubation with IAA alone (lower spectrum). The spectra are centered on the region corresponding to the "dimeric" peak. The relative proportions of the "monomeric" and "dimeric" peaks (peak area expressed in %) are indicated on the corresponding graphs where appropriate.

Figure 5. Mass spectrometry analysis of WT mS100A9 in the presence of divalent cations. **(A)** and **(B)** LC/ESI-TOF-MS and native MS spectra of untreated WT mS100A9 in the presence of 1 mM $CaCl_2$. **(C)** and **(D)** LC/ESI-TOF-MS and native MS spectra of untreated WT mS100A9 in the presence of 1 mM $ZnCl_2$. **(E)** and **(F)** LC/ESI-TOF-MS and native MS spectra of untreated WT mS100A9 in the presence of 1 mM $CaCl_2$ + 1 mM $ZnCl_2$. The relative proportions of the "monomeric" and "dimeric" peaks (peak area expressed in %) are indicated on the LC/ESI-TOF-MS spectra.

Figure 6. Mass spectrometry analysis of the Cys-to-Ala mutants of mS100A9 in the absence or in the presence of divalent cations. **(A)** SDS-PAGE analysis of WT and mutant mS100A9 in the four different ionic conditions tested in the study. The sample deposited in each lane is indicated above the gels. **(B)** Superimposition of the LC/ESI-TOF-MS deconvoluted spectra obtained for untreated C111A mutant in the absence of ions (upper spectrum), in the presence of 1 mM $CaCl_2$ (upper middle spectrum), in the presence of 1 mM $ZnCl_2$ (lower middle spectrum), or in the presence of

1 mM $CaCl_2$ + 1 mM $ZnCl_2$ (lower spectrum). **(C)** Same as panel **B** but for mutant C91A. **(D)** Same as panel **B** but for mutant C80A.

Figure 7. Structure of Ca^{2+}/Zn^{2+}-bound mS100A9 C80A and possible models for the disulfide-crosslinked mS100A9 homodimer. (**A**) General overview of the structure of the Ca^{2+}/Zn^{2+}-bound murine S100A9 C80A mutant (mS100A9-C80A) homodimer at 2.35 Å resolution. The two mS100A9-C80A subunits are shown in beige and purple. Calcium and zinc ions are displayed as green and yellow spheres, respectively. The zinc coordinating residues are depicted as sticks. The structure of the WT mS100A9 protein determined in this study has been superimposed for comparison (dark blue cartoon). **(B)** Canonical homodimer conformation of mS100A9 as observed in our crystal structure. In this configuration, only the two Cys111 from each monomer may reach out to form an intramolecular SS bridge although they are separated by more than 50Å, due in part to the side chains protruding from both helices H4. Inter-subunit interaction of Cys111 with Cys80 or Cys91 from the other subunit would require partial unfolding of the second S100A9 protomer (interactions indicated with a question mark).

1311

1312

	mS100A9 (WT) (native)	mS100A9 (WT) (anomalous)	mS100A9 (WT) (anomalous)	mS100A9 (C80A) (native)
Data collection				
Diffraction source	ID23eh1, ESRF	ID23eh1, ESRF	ID23eh1, ESRF	X06DA, SLS
Wavelength (Å)	1.27	1.27	1.30	1.28
Space group	C2	C2	C2	C2
a, *b*, *c* (Å)	72.84, 40.62, 53.09	72.84, 40.62, 53.09	72.97, 40.65, 53.17	73.61, 38.80, 53.17
α, β, γ (°)	90, 125, 90	90, 125, 90	90, 124.99, 90	90, 124.75, 90
Mosaicity (°)	0.28	0.28	0.28	0.41
Resolution range (Å)	80 – 1.45 (1.51 – 1.45)	80 – 1.45 (1.51 – 1.45)	80 – 1.5 (1.57 – 1.5)	80 – 2.35 (2.44 – 2.35)
Total No. of reflections	141507 (13504)	143258 (13475)	130241 (14794)	34129 (3573)
No. of unique reflections	22267 (2406)	43051 (4657)	39043 (4809)	5224 (550)
Completeness (%)	97.6 (92.8)	96.9 (91.3)	96.9 (93.9)	98.5 (98.6)
Redundancy	6.35 (5.6)	3.3 (2.9)	3.3 (3.1)	6.5 (6.5)
$I / \sigma(I)$	14.57 (1.93)	14.18 (1.52)	16.31 (1.57)	8.73 (2.33)
R_{meas}	5.9 (78.2)	4.4 (77.1)	3.8 (78.6)	13.2 (84.3)
Wilson B factor (Å^2)	30.3	30.3	32.4	43.5
Refinement				
Resolution range (Å)	43 – 1.45			43 – 2.35
No. of unique reflections	22210			5198
Final R_{work} / R_{free} (%)	17.57 / 19.95			26.80 / 30.54
No. of non-H atoms				
Protein	868			867
Ions	9			20
Water	97			6
Total	974			893
R.m.s. deviations				
Bonds (Å)	0.004			0.002
Angles (°)	0.720			0.461
Average B factors (Å^2)				
Protein	38.7			66.8
Ions	27.1			76.3
Water	47.1			59.3
Ramachandran plot				
Favored regions (%)	99.06			99.06
Allowed regions (%)	0.94			0.94
Outliers (%)	0			0

1313

1314 **Table 1.** Data collection and refinement statistics.

Zn-ligand bond distances

Zn site	Ligand	Bond distance (Å)	Monodentate vs Bidentate ligand
Zn1/Zn3	His21	1.92	nr
	Asp31	1.89 / 2.81	bidentate
	His92	1.99	nr
	His96	2.01	nr
Zn2/Zn4	Glu65	1.90	monodentate
	His103	2.08	nr
	His105	2.06	nr
	His107	2.04	nr

Zn-ligand bond angles

Zn site	Ligand 1	Ligand 2	Angle (°)
Zn1/Zn3	His21	Asp31	124.3
	His21	His92	107.4
	His21	His96	109.1
	Asp31	His92	114.2
	Asp31	His96	95.4
	His92	His96	103.8
Zn2/Zn4	Glu65	His103	111.9
	Glu65	His105	106.8
	Glu65	His107	118.5
	His103	His105	114.2
	His103	His107	104.6
	His105	His107	100.6

Table 2. Zn^{2+}-ligand bond distances and angles measured for the two different types of Zn-binding sites encountered in mS100A9 crystal structure. nr: not relevant.

Sample		Ca	Cr	Mn	Fe	Co	Ni	Cu	Zn
Buffer 1	ppb	151	0.061	Nd	Nd	0.122	4.760	0.554	1.787
	µM	3.764	0.001	Nd	Nd	0.002	0.081	0.009	0.027
mS100A9	ppb	146	0.139	Nd	Nd	0.088	7.851	3.490	22.010
	µM	3.644	0.003	Nd	Nd	0.001	0.133	0.055	0.336
	equiv./A9	0.018	1.34e-5	Nd	Nd	7.46e-6	7e-4	3e-4	0.002
Control SLRS-6									
SLRS-6	ppb	9161.5	0.260	2.218	85.513	0.059	0.612	25.76	1.960
Certified values SLRS-6	ppb	8770	0.252	2.12	84.5	0.053	0.617	24.0	1.76
	SD (ppb)	200	0.012	0.10	3.6	0.012	0.022	1.8	0.12

Table 3. Metal content of purified WT mS100A9 as analyzed by ICP-MS. Each sample was analyzed only once (averaging over 3 replicates). Metal content is given in parts per billion (ppb), in concentration (µM), and as molar equivalents with respect to mS100A9. Nd indicates that the concentration was below detection limit and could not be determined. Certified water SLRS-6 was used as a control (both the values measured in our experiments, the certified values and the standard deviation SD on certified values are indicated for SLRS-6).

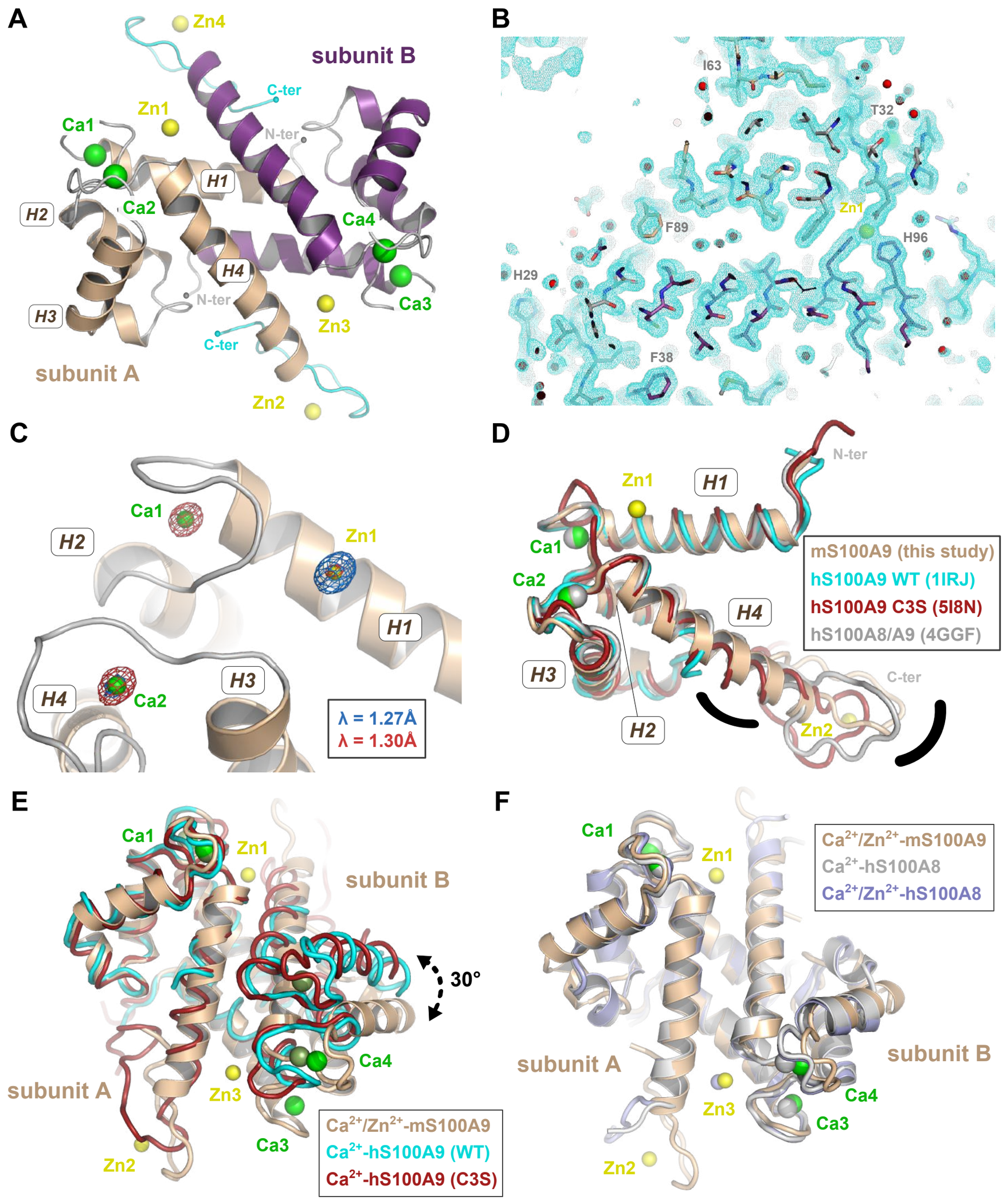
A
Zn4
subunit B
C-ter
Zn1
Ca1
N-ter
H1
H2
Ca2
Ca4
H4
N-ter
Ca3
H3
Zn3
C-ter
subunit A
Zn2
B
I63
T32
Zn1
F89
H96
H29
F38
C
Ca1
H2
Zn1
H1
H4
Ca2
H3
λ = 1.27Å
λ = 1.30Å
D
N-ter
Zn1
H1
Ca1
Ca2
H4
H3
C-ter
H2
Zn2
mS100A9 (this study)
hS100A9 WT (1IRJ)
hS100A9 C3S (5I8N)
hS100A8/A9 (4GGF)
E
Ca1
Zn1
subunit B
30°
Ca4
subunit A
Zn3
Ca3
Zn2
Ca2+/Zn2+-mS100A9
Ca2+-hS100A9 (WT)
Ca2+-hS100A9 (C3S)
F
Ca1
Zn1
Ca2+/Zn2+-mS100A9
Ca2+-hS100A8
Ca2+/Zn2+-hS100A8
subunit A
subunit B
Ca4
Zn3
Ca3
Zn2

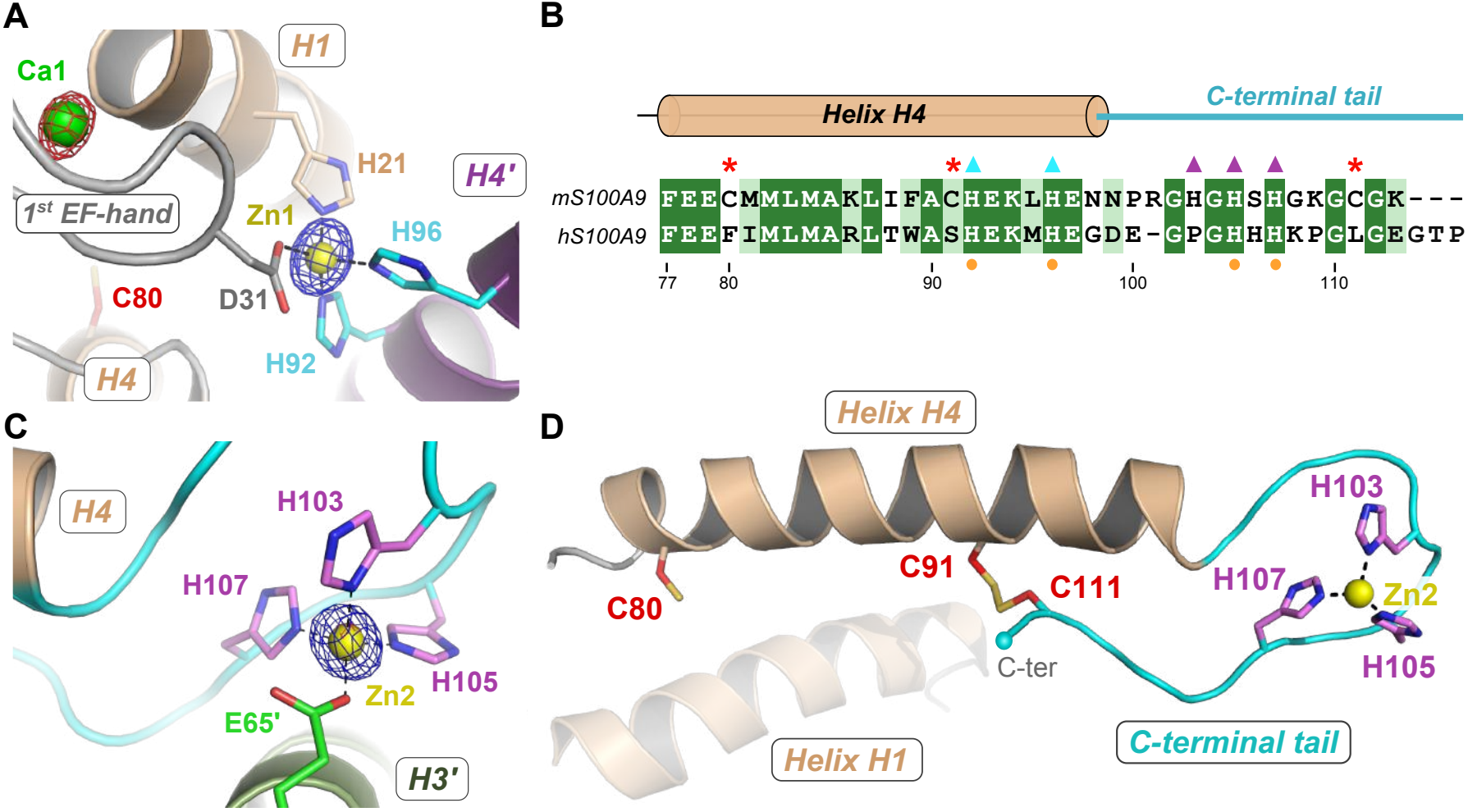
A
Ca1
H1
H21
H4'
1st EF-hand
Zn1
H96
C80
D31
H92
H4
B
Helix H4
C-terminal tail
mS100A9 FEECMMLMAKLIFACHEKLHENNPRGHGHSHGKGCGK---
hS100A9 FEEFIMLMARLTWASHEKMHEGDE-GPGHHHKPGLGEGTP
77
80
90
100
110
C
H4
H103
H107
H105
Zn2
E65'
H3'
D
Helix H4
C80
C91
C111
H103
H107
Zn2
H105
C-ter
Helix H1
C-terminal tail

A

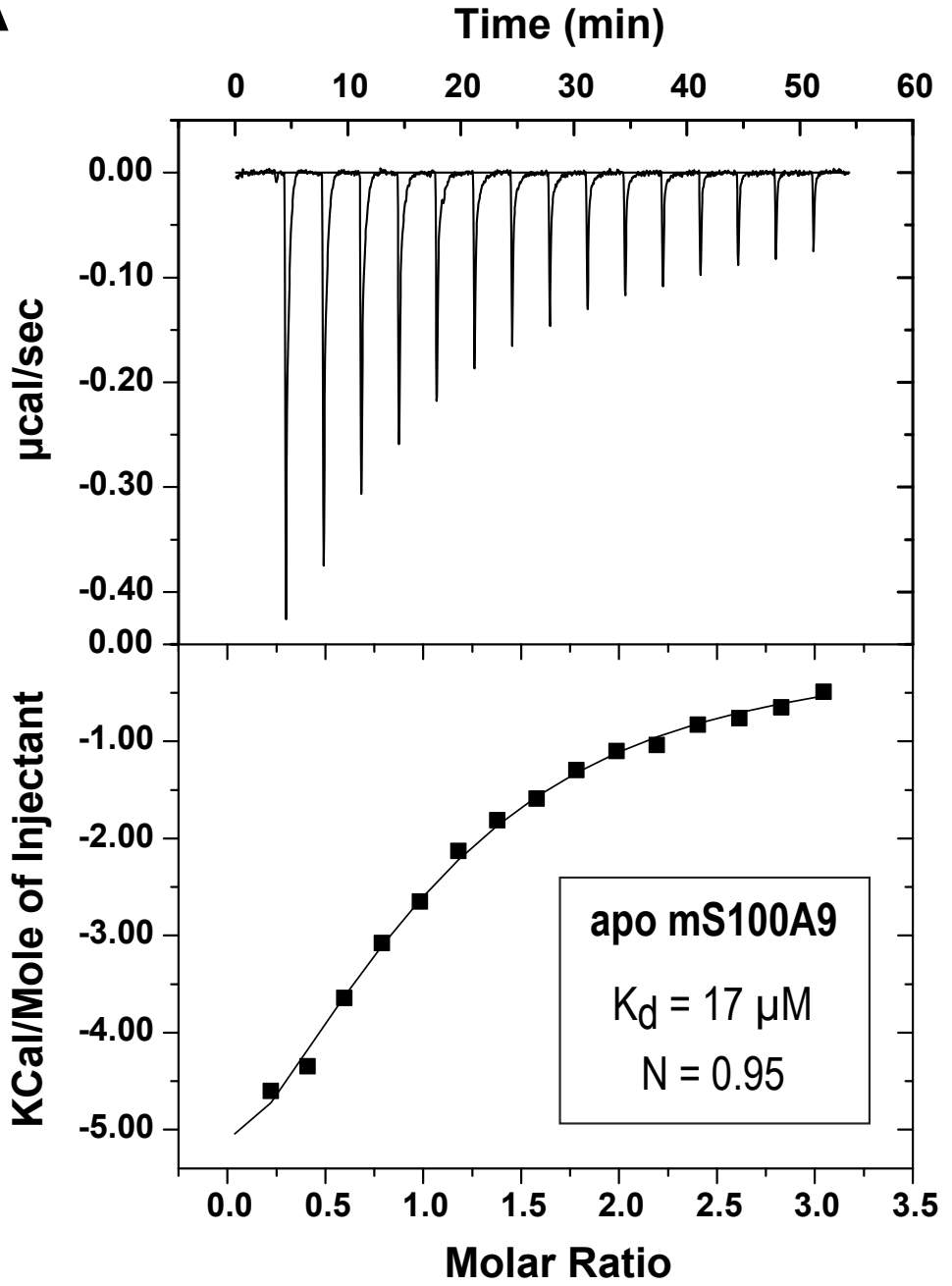
Time (min)
µcal/sec
KCal/Mole of Injectant
Molar Ratio
apo mS100A9
K_d = 17 µM
N = 0.95

B

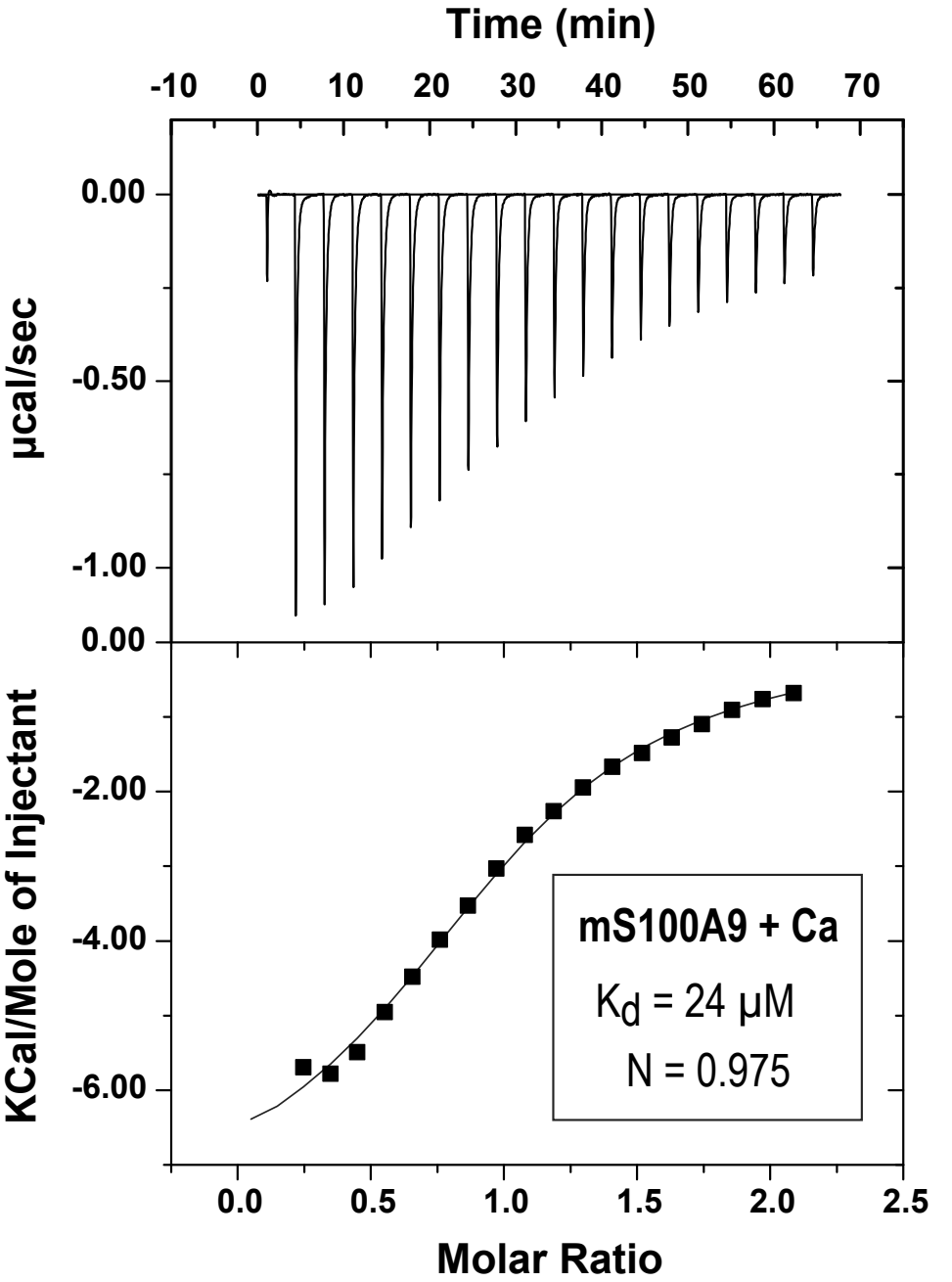
Time (min)
µcal/sec
KCal/Mole of Injectant
Molar Ratio
mS100A9 + Ca
K_d = 24 µM
N = 0.975

C

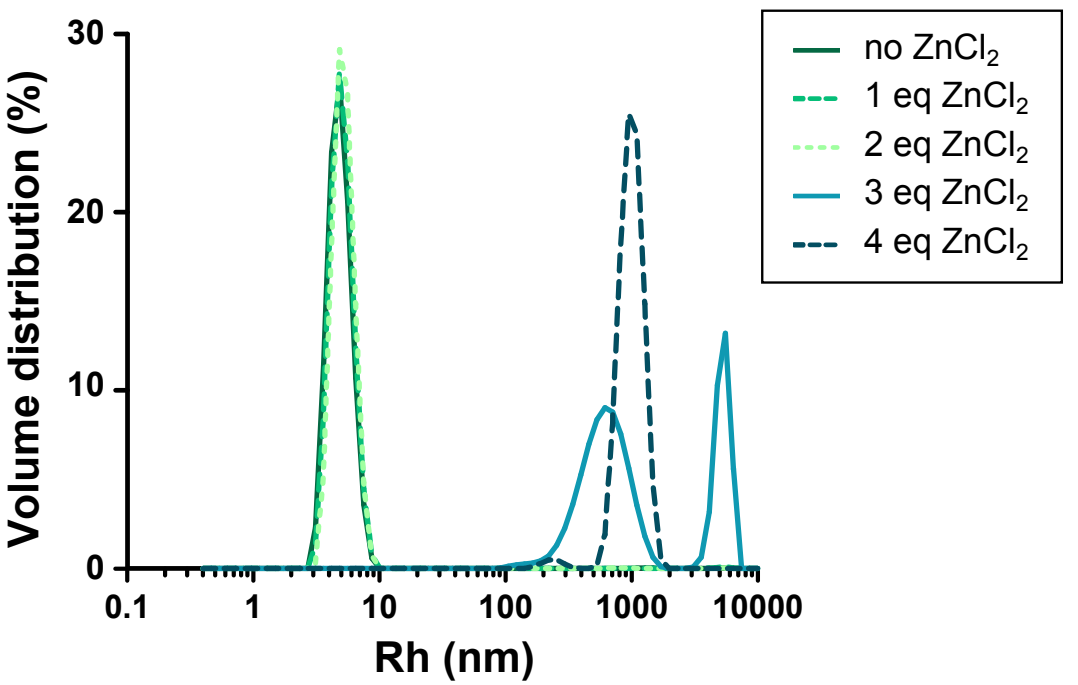
apo mS100A9
Volume distribution (%)
Rh (nm)
no $ZnCl_2$
1 eq $ZnCl_2$
2 eq $ZnCl_2$
3 eq $ZnCl_2$
4 eq $ZnCl_2$

D

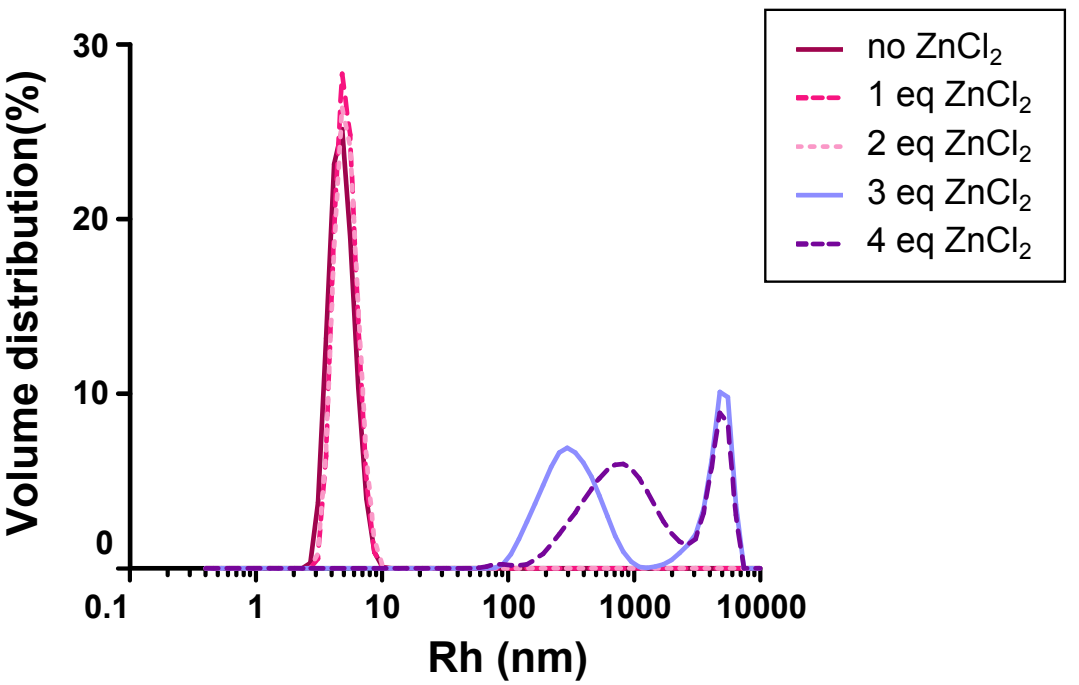
mS100A9 + $CaCl_2$
Volume distribution(%)
Rh (nm)
no $ZnCl_2$
1 eq $ZnCl_2$
2 eq $ZnCl_2$
3 eq $ZnCl_2$
4 eq $ZnCl_2$

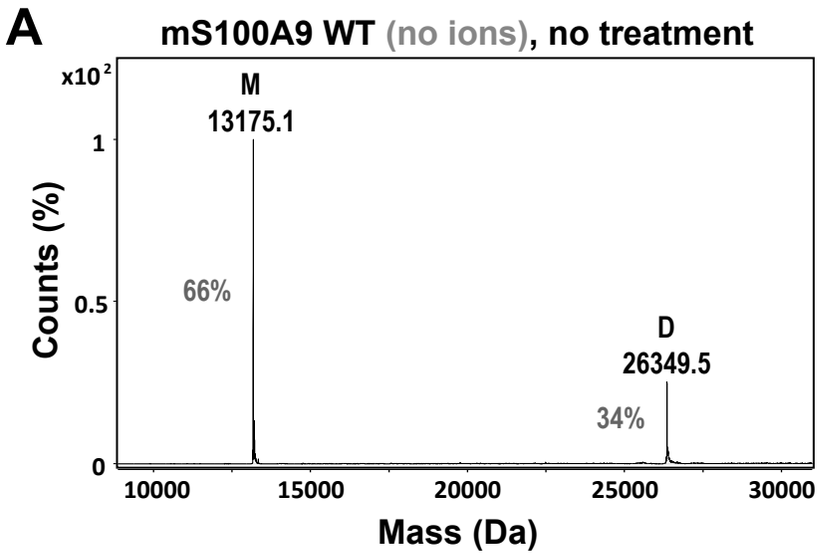
A
mS100A9 WT (no ions), no treatment
x10 2
M
13175.1
66%
D
26349.5
34%
Counts (%)
Mass (Da)

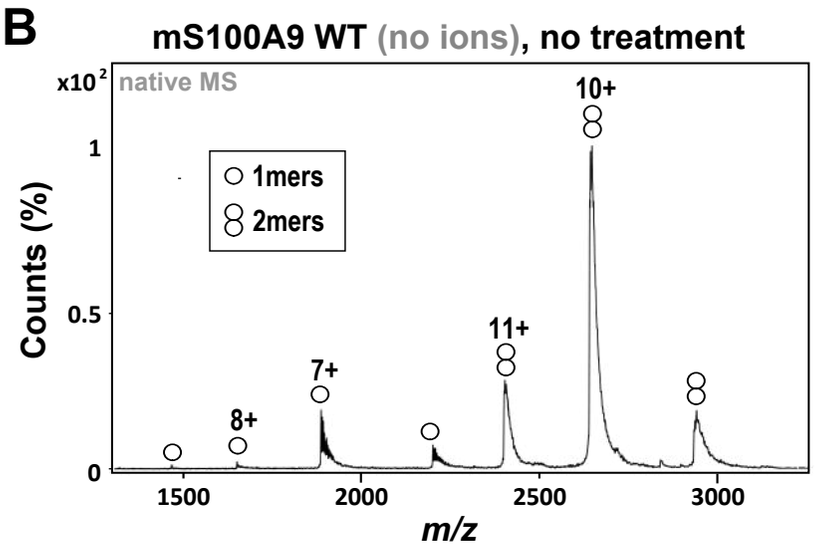
B
mS100A9 WT (no ions), no treatment
native MS
1mers
2mers
8+
7+
11+
10+
Counts (%)
m/z

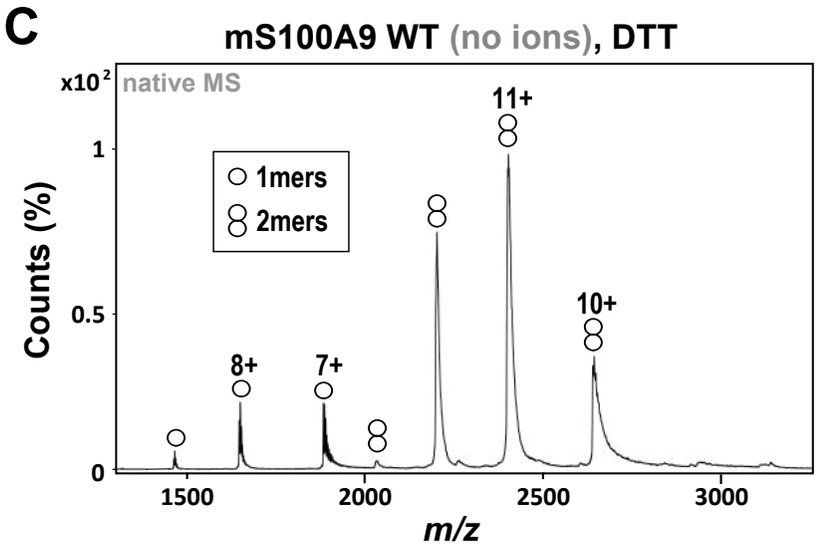
C
mS100A9 WT (no ions), DTT
native MS
1mers
2mers
8+
7+
11+
10+
Counts (%)
m/z

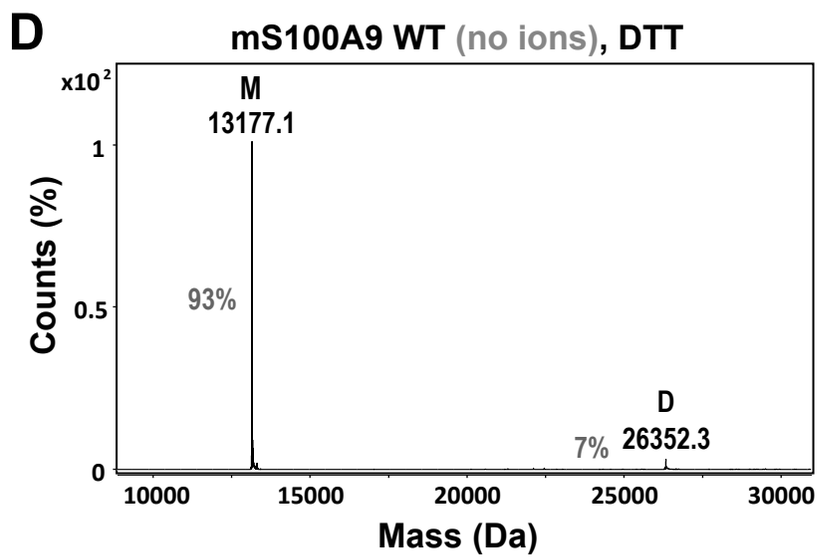
D
mS100A9 WT (no ions), DTT
M
13177.1
93%
D
26352.3
7%
Counts (%)
Mass (Da)

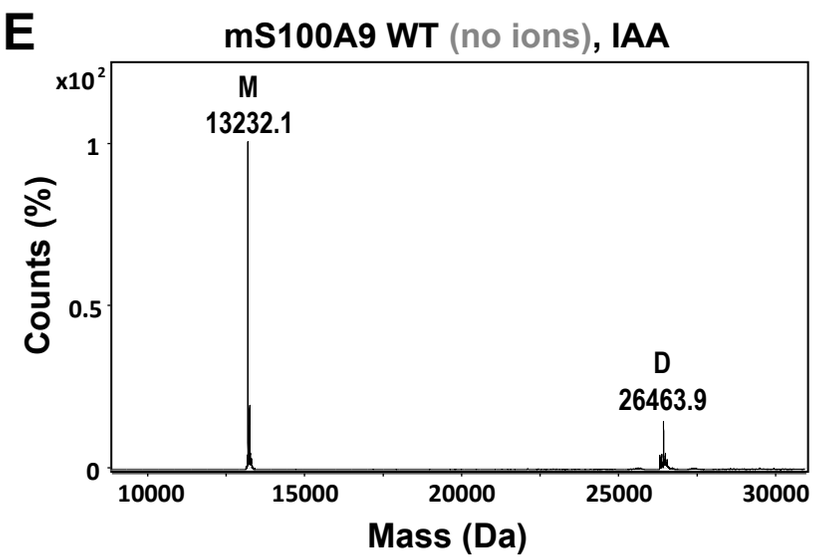
E
mS100A9 WT (no ions), IAA
M
13232.1
D
26463.9
Counts (%)
Mass (Da)

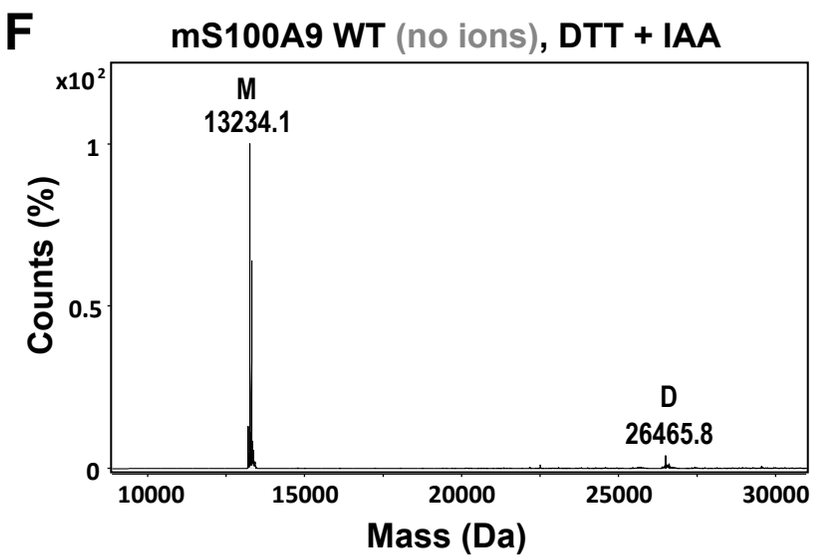
F
mS100A9 WT (no ions), DTT + IAA
M
13234.1
D
26465.8
Counts (%)
Mass (Da)

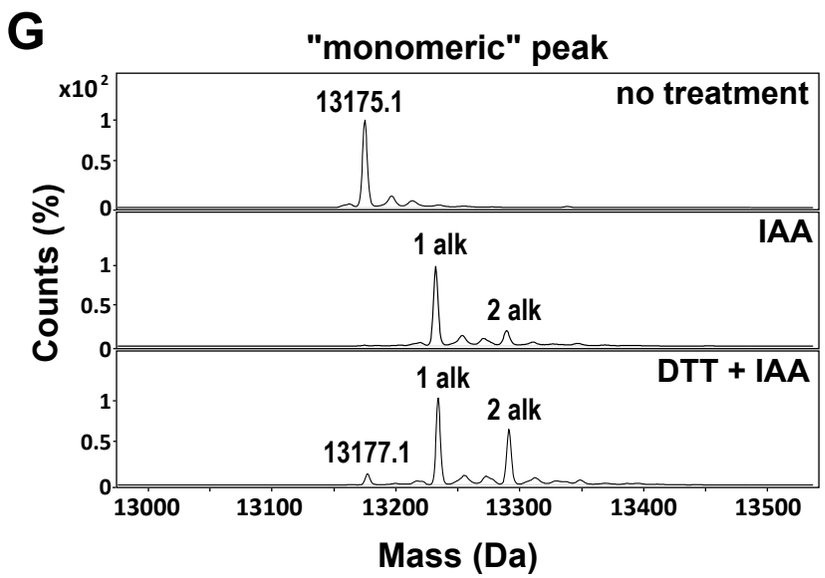
G
"monomeric" peak
no treatment
13175.1
IAA
1 alk
2 alk
DTT + IAA
1 alk
2 alk
13177.1
Counts (%)
Mass (Da)

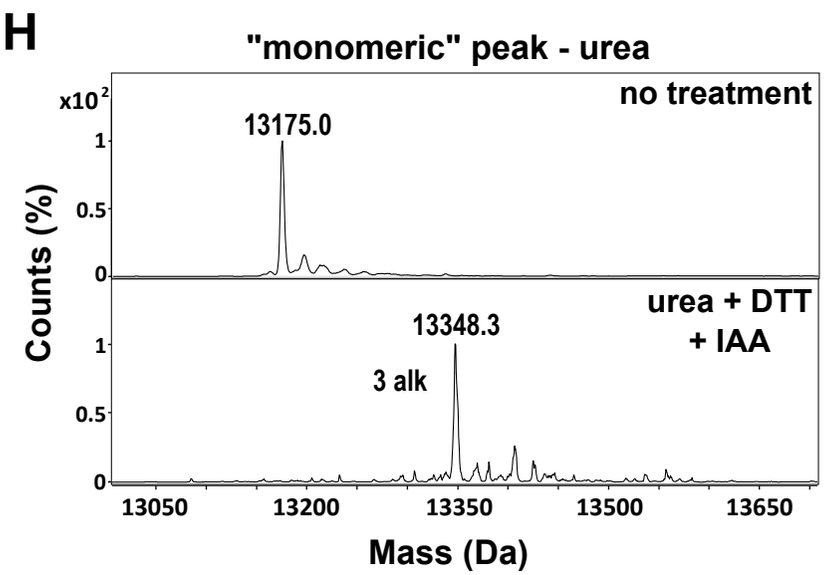
H
"monomeric" peak - urea
no treatment
13175.0
urea + DTT
+ IAA
13348.3
3 alk
Counts (%)
Mass (Da)

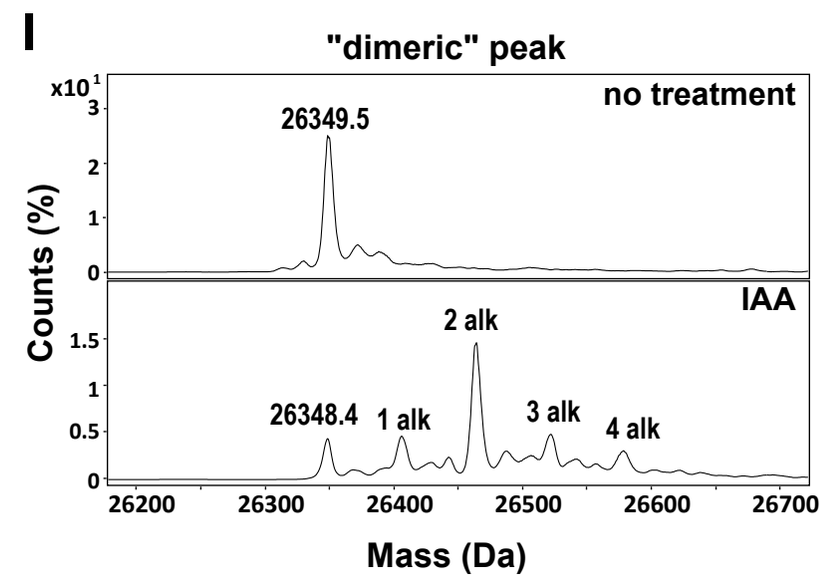
I
"dimeric" peak
no treatment
26349.5
IAA
2 alk
26348.4
1 alk
3 alk
4 alk
Counts (%)
Mass (Da)

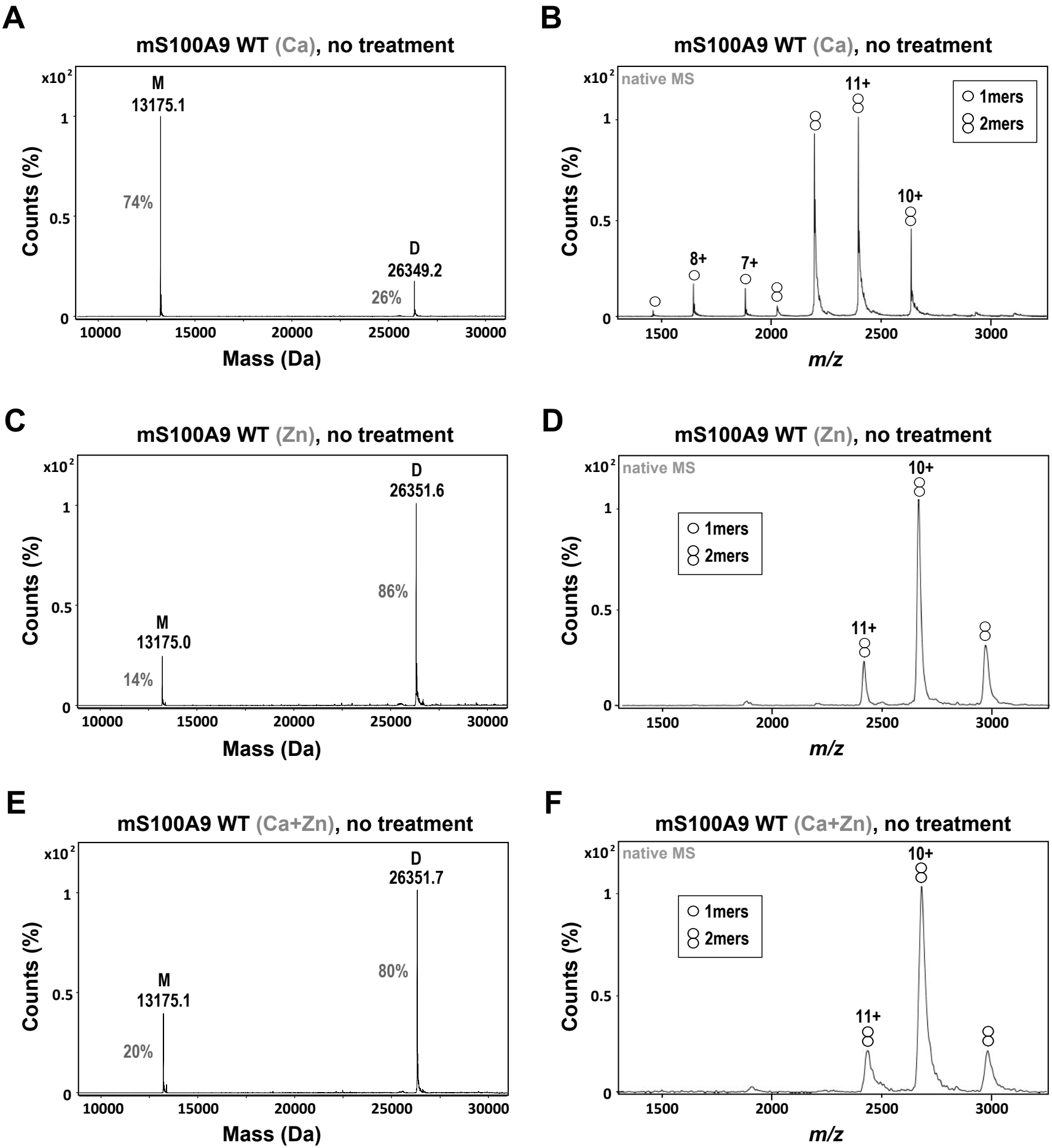
A
mS100A9 WT (Ca), no treatment
x10²
M
13175.1
74%
D
26349.2
26%
Counts (%)
Mass (Da)
B
mS100A9 WT (Ca), no treatment
native MS
1mers
2mers
11+
10+
8+
7+
Counts (%)
m/z
C
mS100A9 WT (Zn), no treatment
D
26351.6
86%
M
13175.0
14%
Counts (%)
Mass (Da)
D
mS100A9 WT (Zn), no treatment
native MS
1mers
2mers
10+
11+
Counts (%)
m/z
E
mS100A9 WT (Ca+Zn), no treatment
D
26351.7
80%
M
13175.1
20%
Counts (%)
Mass (Da)
F
mS100A9 WT (Ca+Zn), no treatment
native MS
1mers
2mers
10+
11+
Counts (%)
m/z

A

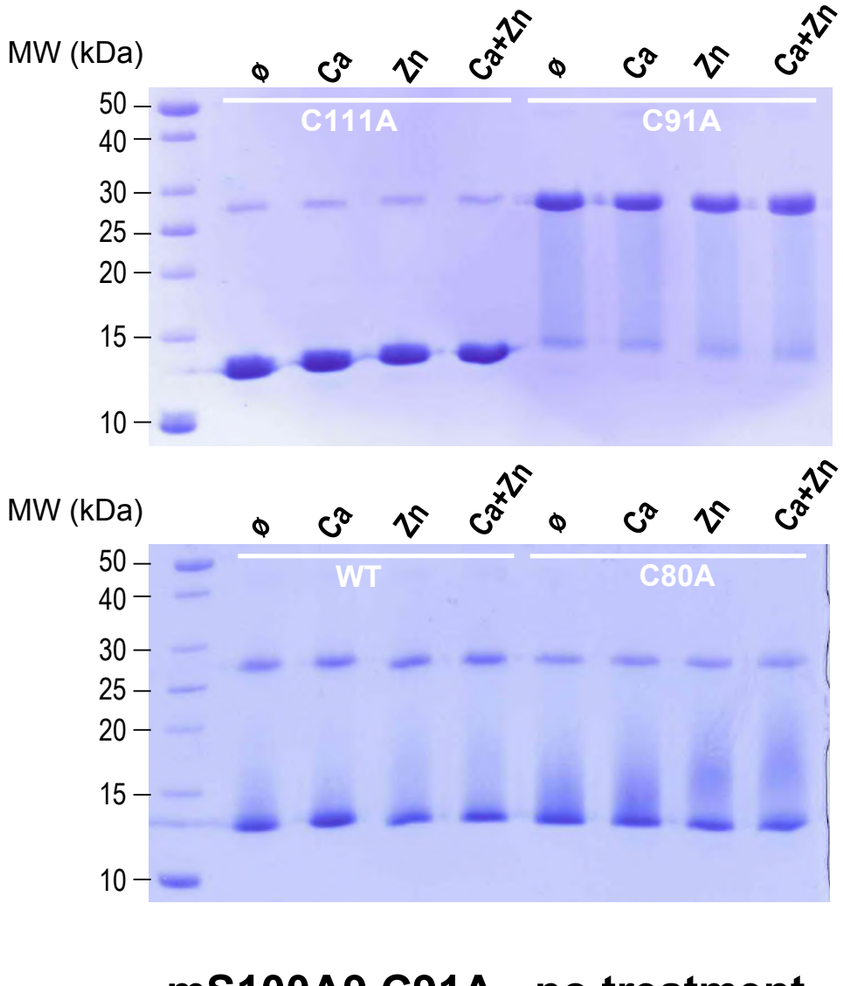
MW (kDa)
ø
Ca
Zn
Ca+Zn
ø
Ca
Zn
Ca+Zn
C111A
C91A
50
40
30
25
20
15
10
MW (kDa)
ø
Ca
Zn
Ca+Zn
ø
Ca
Zn
Ca+Zn
WT
C80A
50
40
30
25
20
15
10

B

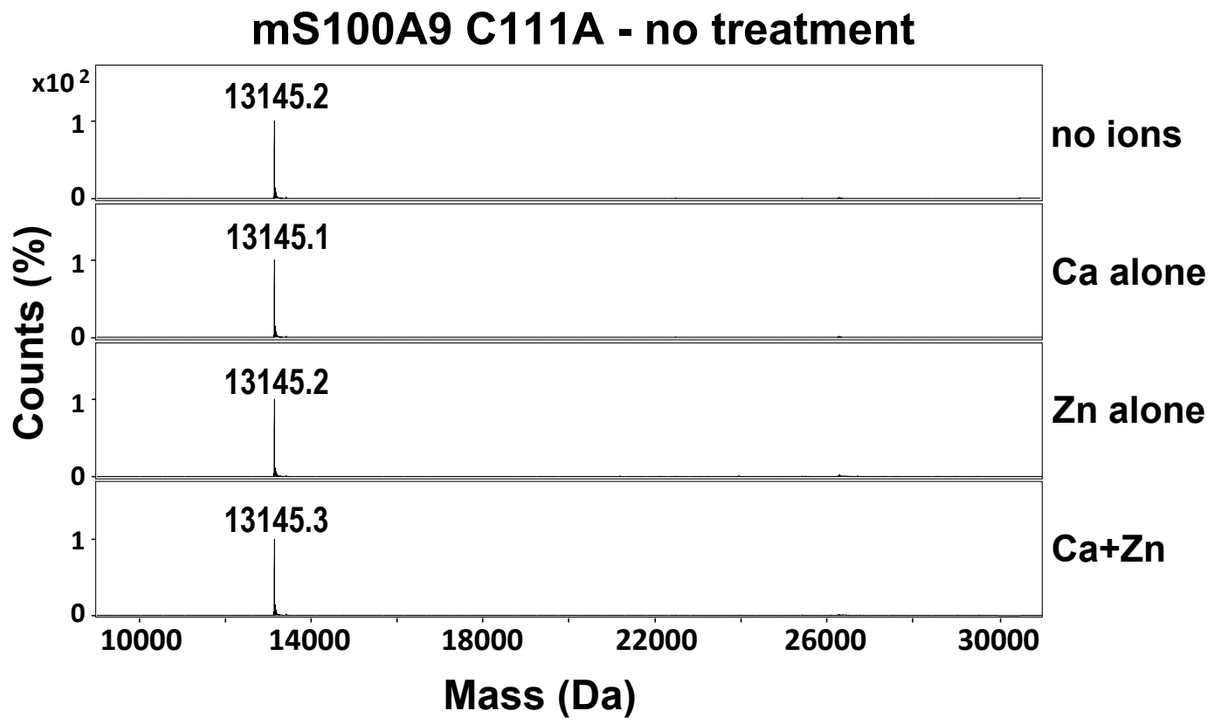
mS100A9 C111A - no treatment
x10 2
13145.2
13145.1
13145.2
13145.3
no ions
Ca alone
Zn alone
Ca+Zn
Counts (%)
10000
14000
18000
22000
26000
30000
Mass (Da)

C

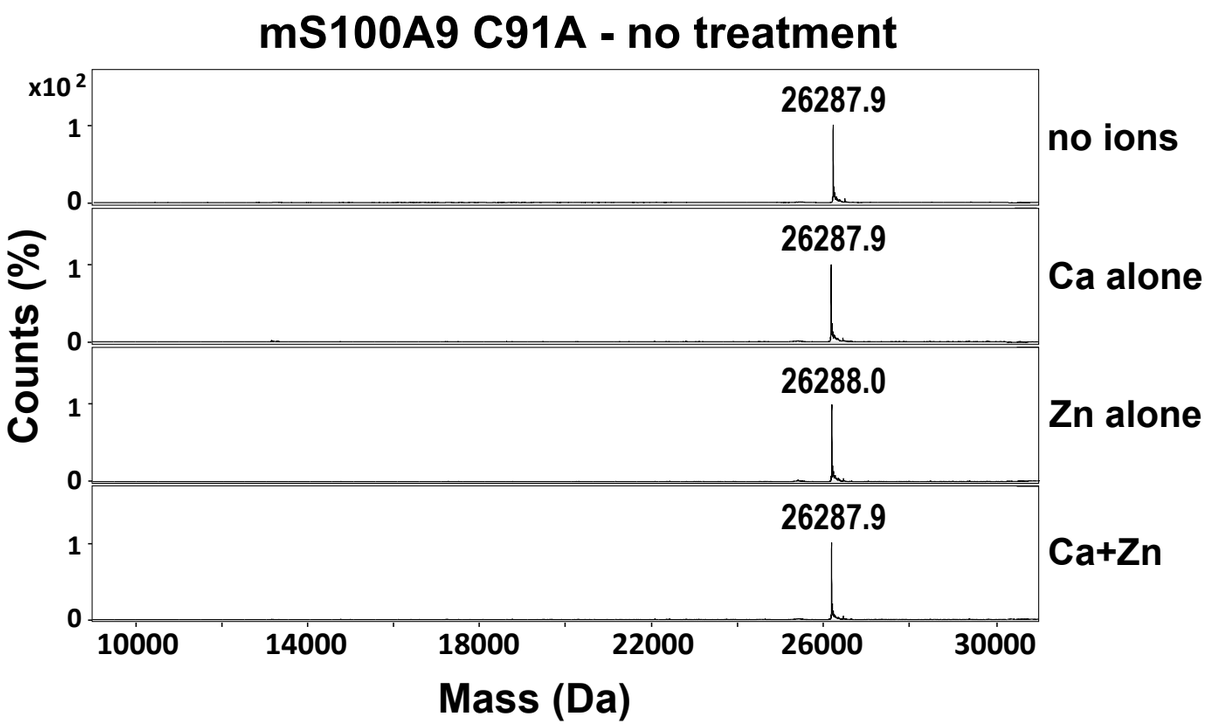
mS100A9 C91A - no treatment
x10 2
26287.9
26287.9
26288.0
26287.9
no ions
Ca alone
Zn alone
Ca+Zn
Counts (%)
10000
14000
18000
22000
26000
30000
Mass (Da)

D

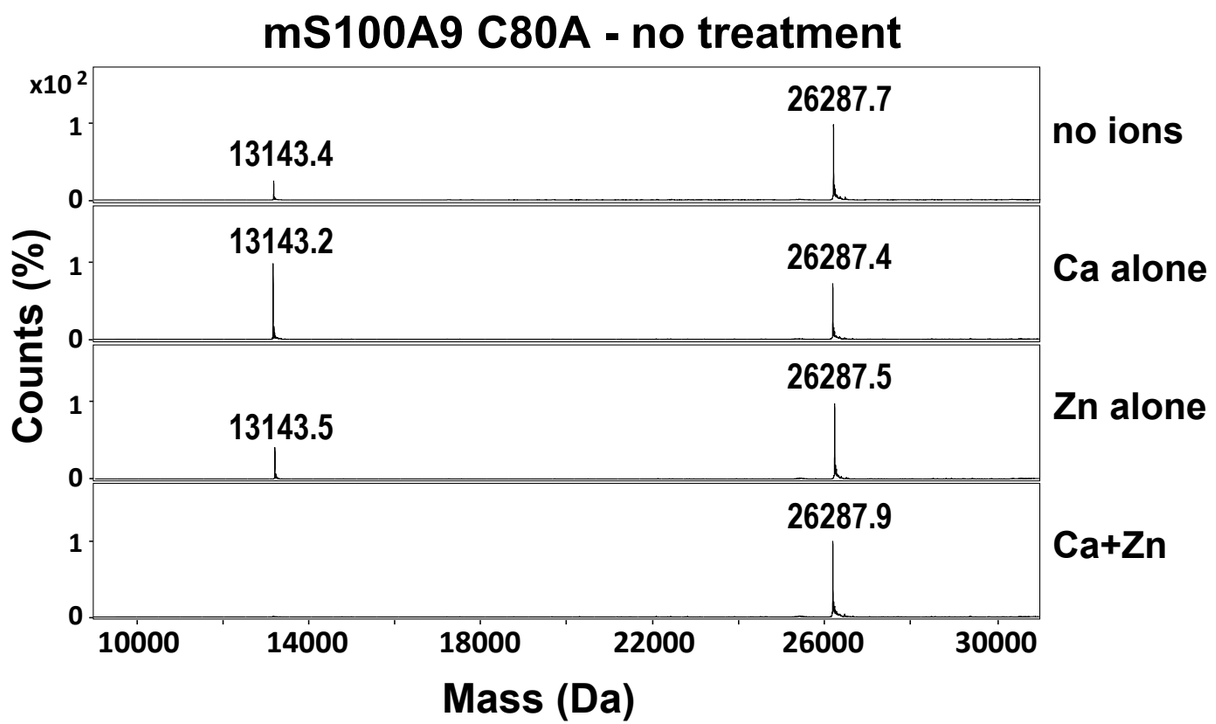
mS100A9 C80A - no treatment
x10 2
26287.7
13143.4
13143.2
26287.4
13143.5
26287.5
26287.9
no ions
Ca alone
Zn alone
Ca+Zn
Counts (%)
10000
14000
18000
22000
26000
30000
Mass (Da)

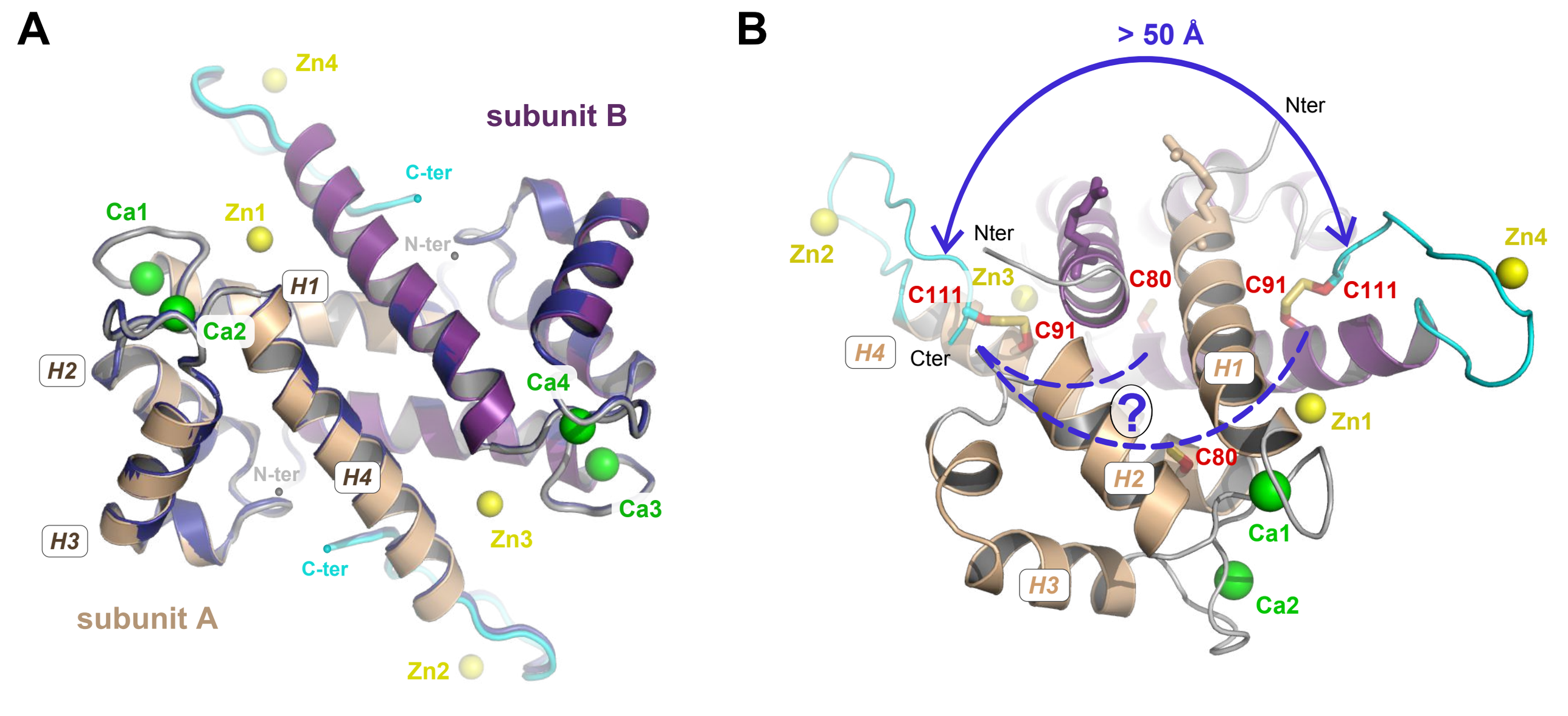
A
Zn4
subunit B
C-ter
Ca1
Zn1
N-ter
H1
Ca2
H2
Ca4
N-ter
H4
Ca3
H3
Zn3
C-ter
subunit A
Zn2
B
> 50 Å
Nter
Nter
Zn2
Zn3
C80
C91
C111
Zn4
C111
C91
H4
Cter
H1
?
Zn1
C80
H2
Ca1
H3
Ca2